UNIVERSITY OF BELGRADE
FACULTY OF TECHNOLOGY AND METALLURGY

Ramadan Al-Mukhtar Dukali

SYNTHESIS AND CHARACTERIZATION OF SCINTILLATION COMPOSITE MATERIALS WITH POLYMER MATRIX

Doctoral Dissertation

Belgrade, 2014

UNIVERZITET U BEOGRADU
TEHNOLOŠKO-METALURŠKI FAKULTET

Ramadan Al-Mukhtar Dukali

SINTEZA I KARAKTERIZACIJA SCINTILACIONIH KOMPOZITNIH MATERIJALA SA POLIMERNOM MATRICOM

Doktorska Disertacija

Beograd, 2014

Supervisor

Dr Vesna Radojević, associate professor, University Of Belgrade

Faculty of Technology and Metallurgy

Member of Committee

Dr Radoslav Aleksić, full professor, University Of Belgrade

Faculty of Technology and Metallurgy

Dr Petar Uskoković, full professor, University Of Belgrade

Faculty of Technology and Metallurgy

Dr Aleksandar Grujić, associate Research Professor, University Of Belgrade,
Institute of Chemistry, Technology and Metallurgy

Dr Jelena Lamovec, assistant Research Professor, University Of Belgrade,
Institute of Chemistry, Technology and Metallurgy

Date:_____

ACKNOWLEDGEMENTS

It is a great pleasure for me to express my sincere gratitude to the people whose generous assistance and support this research.

I would like to take this opportunity to express my sincere thanks to my research advisor, Dr. Vesna Radojevic for all her guidance, direction and support during the evolvement of this thesis.

I am totally indebted to Dr. Radoslav Aleksic, Head of Department of Materials Science and Engineering and my committee member for all his help and resourceful suggestions.

I would like to acknowledge Dr. Petar Uskokovic, Dr. Aleksandar Grujic and Dr. Jelena Lamovec my thesis examiners for their insightful suggestions and comments on my thesis.

Special thanks to Dr. Dusica Stojanovic for her encouragements in my research life and technical support in experiments.

SINTEZA I KARAKTERIZACIJA SCINTILACIONIH KOMPOZITNIH MATERIJALA SA POLIMERNOM MATRICOM

Rezime

Predmet ove doktorske disertacije obuhvata istraživanja u oblasti funkcionalnih optoelektronskih kompozitnih materijala s polimernom matricom za primenu u elektronskim tehnologijama kao i u oblasti radiologije, dozimetrije, luminiscentnih svetlovoda, lasera i senzora. Indeks refrakcije polimera može biti modifikovan dodavanjem čestica sa velikom vrednošću indeksa refrakcije. Ovaj tip modifikacije se vrši na materijalima za detekciju jonizujućeg zračenja, gde se čestice neorganskih scintilacionih kristala kao što su BaF_2, CeF_3, CsI, $Bi_{12}GeO_{20}$ (BGO), ili $Bi_{12}SiO_{20}$ (BSO) ugrađuju u matricu polimera. Tokom dosadašnjih istraživanja u ovoj oblasti fluoridi i BGO su pokazali dobre rezultate, dok BSO poseduje slična svojstva kao i BGO, ali je jeftiniji. Ugradnjom BSO u polimerni kompozit dobio bi se dostupniji materijal šireg opsega primene.

U eksperimentalnom delu ovog doktorata izvedeno je procesiranje i karakterizacija kompozitnog materijla PMMA- $Bi_{12}SiO_{20}$ (BSO). Procesom livenja iz rastvora dobijeni su tanki filmovi čistog PMMA i kompozita sa 0.5 and 1.0 mas% $Bi_{12}SiO_{20}$ čestica. U cilju ispitivanja morfologije i structure kao i termijskih, optičkih i mehaničkih svojstava, karakterizacija polaznh komponenti i dobijenih kompozita izvedena je primenom metoda XRD, FTIR, Raman spectroskopije, SEM, DSC, ispitivanjem zatezanjem, nanoindentacijom i spektroskopskom elipsometrijom. Ispitivanje spektroskopskom elipsometrijom pokazalo je da je indeks refrakcije kompozita veći u odnosu na čist polimer i raste sa povećanjem sadržaja BSO. Nanoindentacija i ispitivanje zatezanjem pokazali su da mehanička svojstva kompozita rastu sa dodatkom prah BSO. Vrednosti Jungovog modula elastičnosti kao i redukovanog modula elastičnosti i tvrdoće rastu sa povećanjem sadržaja kristalnog BSO. Termijska svojstva ispitivana su metodom DSC. Tempeartura transformacije u staklasto stanje, T_g, raste sa dodatkom BSO u PMMA , kao i sa poveanjem sadržaja BSO praha u kompozitu.

U okviru ove disertacije takođe je izvedeno i ispitano je elektropredenje poli(metilmetakrilata) dopiranog Rodaminom B, koja je veoma perspektivna tehnika za dobijanje foto luminiscentnih nanovlakana. Izveden je proces elektropredenja nanovlakana sa različitim sadržajem Rodamina B od 0,05 mas. % and 2,0 mas. %. Interakcija polimerne matrice vlakana i boje analizirana je primenom metode Furijeove transformacije infracrvenog spektra. Pomoću SEM-a ispitivana je morfologija vlakanakao i veličina i njihova raspodela. Diferencijalnom skenirajućom kalorimetrijom analizirana su termička svojstva a optička svojstva tehnikom laserski indukovane fluorescencije (LIF). Dobijena su vlakna glatke površine i bez mehurova. Analiza diferncijalnom skenirajućom kalorimetrijomje pokazala da T_g raste sa porastom sadržaja Rodamina B u poli(metilmetakrilat)u do koncentracije od 0, 5 mas. %, a zatim opada. Pri ispitivanju emisionog fluorescentnog spektra nanovlakana, maksimalna fluorescentna emisija je ostvarena pri sadržaju Rodamina B od c = 0, 2 mas. %.

Ključne reči: Kompozitni materijali, Scintilacija, Fluorescencija, nanovlakna

Naučna oblast: Hemija i hemijska tehnologija, Nauka o materijalima i inženjerstvo materijala

UDK: 66.017

SYNTHESIS AND CHARACTERIZATION OF SCINTILLATION COMPOSITE MATERIALS WITH POLYMER MATRIX

Abstract

The aim of this dissertation was the research of functional optoelectronic composite materials with polymer matrix for use in electronic technologies and radiology, dosimetry, luminescent lightguides, lasers and sensors. Refractive index of polymers could be modified with embedded particles with high index of refraction. The modification could be done by embedding in polymer crystals like BaF_2, CeF_3, CsI, $Bi_{12}GeO_{20}$ (BGO), or $Bi_{12}SiO_{20}$ (BSO) – materials for the detection of ionization radiation. Good results were obtained with fluorides and BGO, wile BSO has similar properties, but it is less expensive. So, with embedding BSO in polymer matrix the most available composite material will be composed. Poly (methyl methacrylate) (PMMA) was chosen as polymer matrix because of excellent optical properties. It is transparent in the visible range of electromagnetic radiation.

In this dissertation processing and characterization of polymer composite material PMMA-$Bi_{12}SiO_{20}$ (BSO) was carried out. Thin films of pure PMMA and composites with 0.5 and 1.0 wt% of $Bi_{12}SiO_{20}$ powder were made using solution casting method. Characterization of starting components and composites was performed with XRD, FTIR, Raman spectroscopy, SEM, DCS, tensile tests, nanoindentation and spectroscopic ellipsometry method in order to obtain information of their morphology, structure, thermal stability, mechanical and optical properties. Refractive index measurements using spectroscopic ellipsometry method have shown that refractive index of composites increases with the powder content. Nanoindentation and tensile tests have shown mechanical improvements with the addition of the crystal through

Young's and reduced Young's modulus and hardness values. DSC analysis has shown an increase in *Tg* for composite with BSO.

The electrospinning of Rhodamine B (RhB) –doped poly (methyl methacrylate) (PMMA) is presented as promising technique for processing photo luminescent nanofibers. Nanofibers with concentrations of RhB in PMMA between 0.05 wt% and 2.0 wt% were studied. The FTIR spectrum, fiber morphology, thermal properties and optical properties of the nanofibers were investigated. The smooth, bead- free and nonporous nanofibers were obtained. Differential scanning calorimetry (DSC) results revealed that the T_g increased with increasing of Rh B content up to a 0.5 wt% and beyond that decreased. The laser induced fluorescence (LIF) technique was used to study the fluorescence properties of the nanofibers. The maximum fluorescence emission was observed at a concentration of RhB of c = 0.2 wt%.

Key words: Composite materials, Scintillation, Fluorescence, Nanofibers
Academic Expertise: Chemistry and Chemical Technology

Field of Academic Expertise: Chemistry and Chemical engineering**,** Materials Science and Engineering

UDC 66.017

TABLE OF CONTENT

INTRODUCTION

Functional composites represent very attractive class of materials, which have become center of many research projects throughout the world [1]. Their physical and chemical properties show sensitivity to changes and have the ability to adapt to the environmental parameters like temperature, pressure, magnetic field, optical wavelength, etc. Composites with polymer matrix are materials of great interest for researchers because their properties can be adjusted by controlling the composition, content and morphology of the particle reinforcement, different processing techniques or by modification of the polymer matrix [2-7]. Material and type of reinforcement (particles, short or continuous fibers) as well as the amount of reinforcement in the composite have a significant influence on the physical and mechanical properties (thermal stability, optical and thermal properties as well as mechanical properties). Also, the addition of reinforcements has an effect on crystalline state of the polymer as well as on the processing parameters. The polymer structure is depended from specific volume. On the other hand the specific volume itself is influenced by the pressure and the temperature history, by the configuration of the polymer chains and flow induced ordering phenomena during flow as well. Consequently, for amorphous and semi-crystalline polymers the morphology has to be related to pressure, temperature, cooling rate and the crystalline state

The general principles in the construction of optical composites involve the intimate mixing of optically functional materials within a processable matrix. Figure 1 shows this type of composite schematically, where the small particles possess the desirable optical properties and the enclosing matrix imparts rocessability in film or fiber forms. Organic materials, especially polymers, have become important class of optical materials due to their high impact-resistance, ease of fabrication, low density, and cost-effective technologies [8,9]. Polymer materials with tunable refraction index

are used as light-guides with adjustable index refraction difference between the core and the cladding [10]. High refractive index polymers are also very useful in optics and photonics due to their ability to reduce reflection losses at interfaces, increasing the light output. Refractive index of polymers could be modified by the addition of particles with high refractive index value. This type of modification is conducted in materials potential for ionizing radiation and particle detection, where heavy scintillating powders like BaF_2, CeF_3, CsI, $Bi_{12}GeO_{20}$ (BGO) [11] or $Bi_{12}SiO_{20}$ (BSO) [12,13] are being implanted in polymer matrix. These composites could be used in EM calorimeters and for detection of soft γ rays, as well as in energy storage systems [11, 15]. Since BSO and BGO show similar scintillation properties, whereas BSO is potentially cheaper, in this study we decided to use BSO crystals [15].

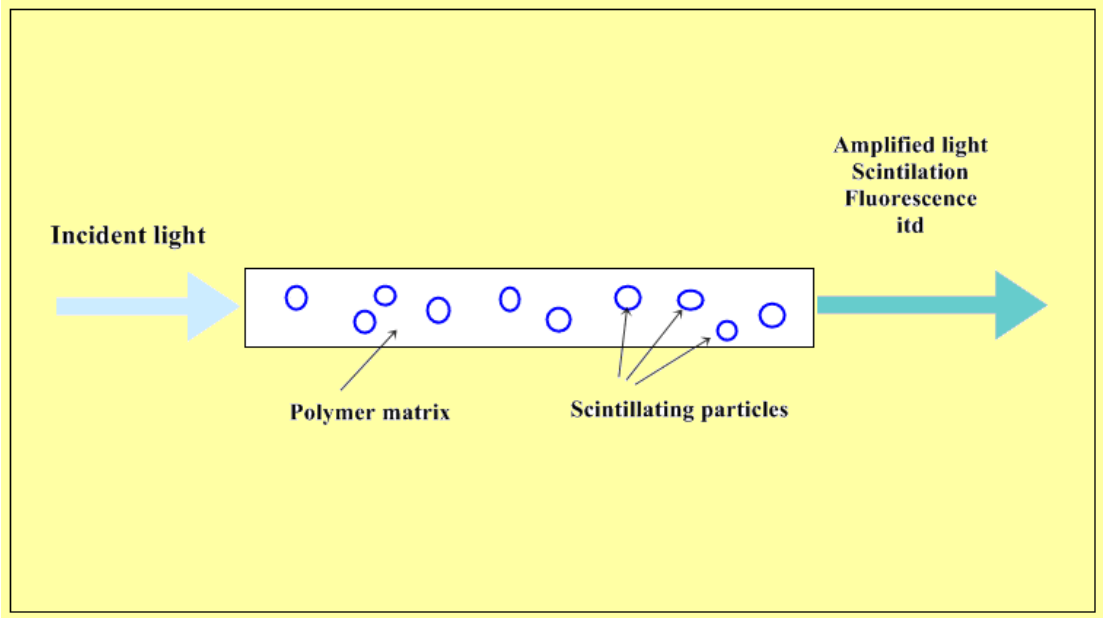

Figure 1 The principle of optically functional composite

In this research, bismuth silicon oxide has been chosen as material for modification of polymer's refractive index. It belongs to a family of sillenites [16-19] along with other compounds presented with chemical formula $Bi_{12}MO_{20}$, where M presents one of four-valence ions Si, Ge, Ti, Mn or a combination of two ions. In BSO-crystals, the refractive index depends on the size of the local electric field caused by the redistribution of photo-electrons [20-22]. High electrical resistivity, strong piezoelectric effect and photoconductivity in the visible region are some of the useful physical

properties shown by BSO crystals [23-25]. Poly (methyl methacrylate) (PMMA) has been chosen in this study as a matrix material. It is a transparent amorphous thermoplastic polymer with numerous excellent properties, such as light weight, high clarity, colorlessness, high impact strength, good insulation but poor fatigue resistance and low utilization temperature [26, 27]. It has been widely used as an optical material [28, 29] and it is considered to be the most commonly used among the methacrylates [30, 31]. Composite material PMMA-BSO is a potential candidate to be used in EM-calorimeters, and X-ray imaging [32] as plastic scintillated fibers because it should have good optical response when exposed to high energy radiation. This research is focused on material processing and influence of BSO powder addition on mechanical properties and refractive index of a composite.

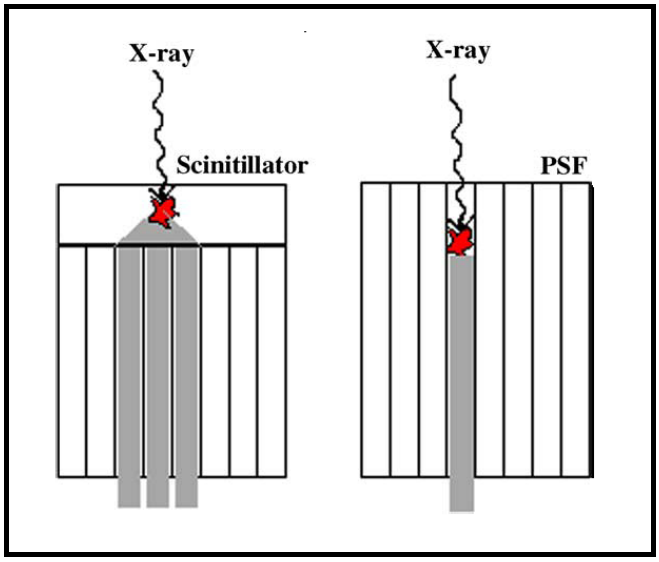

Figure 2. The difference between a scintillation fiber detector and a pure scintillation fiber detector [32].

The aim of the research was to make a composite material with tunable refrative index by introducing heavy inorganic powder (density of BSO 6.80 g/cm^3) in the plastic matrix. Composite material is expected to exhibit higher refractive index value than pure polymer (the refractive index BSO at 633 nm is 2.55) and improved mechanical properties with intact optical properties of bismuth silicon oxide.

Recently, electroluminescent devices based on organic thin layers have attracted much interest due to their potential application as large area light-emitting displays. Organic dyes are also candidates for making LEDs.

Polymer nanofibers offer a great opportunity for applications beyond nano-electronics, [33.34] such as, for membrane materials, [35] tissue scaffolding and other biomedical applications, [36] sensing [37] and as reinforcements in composite materials. [38, 39] Moreover, the properties of these nanoscale polymeric structures make them interesting candidates for the next generation of photonic devices [40, 41]. For example, fibrous dielectric nanostructures could be used as single-mode light waveguides, [42] sensors [43] or building blocks of photonic bandgap materials. [44] Polymer nanofibers could be fabricated by diverse methods, including polymerization in nanoporous templates [45] dip-pen lithography [46] self-assembly, [47] direct drawing from polymer solutions [48] and molding, [49] although only electrospinning [50-55] assures a low cost and high throughput production. Electrospinning is a versatile technique which recently undergone significant development in nanofibers production. The polymer fibers are formed, from the solution, between two electrodes bearing electrical charges of opposite polarity. One of the electrodes is placed into the solution and the other onto a collector. Once ejected out of a metal needle, the charged solution jets evaporated to become fibers which are collected on the collector. The structure and the morphology of the electrospun polymer materials, be it fibers or particles, are determined by a synergistic effect of solution parameters (polymer concentration, solution viscosity, flow rate) and electrostatic forces (applied voltage, distance between the needle and collector).

A major advantage of electrospinning is the possibility to produce hybrid, functional photonic materials by incorporating, *e.g.*, light emitters into the fibers [56-58]. The polymer, the light emitter and the characteristic dimension (diameter of the fibers) can be varied independently, therefore allowing for a wide range of applications. Both organic dye molecules and inorganic materials can be embedded into the fibers. Organic dye-doped polymers have been widely investigated as gain media in solid-state dye lasers [59-62]. Dye molecules which have large absorption and induced emission cross sections due to allowed $\pi - \pi$ transitions are ideal active dopants for the generation and amplification of intense light pulses. Since then, many research groups have synthesized and tested numerous chemical substances that were proved to be good laser dyes. The

dye has, however, to be embedded in a suitable matrix or host. The incorporation of a dye in liquid media adversely affects many thermodynamic and spectroscopic properties of the dye (kinetics of energy up-conversion). The adding of dye in polymer solution changes the viscosity of the solution and hence, influence the process of electrospinning.

Thermoplastic PMMA is considered as one of the most efficient dye matrices with excellent optical, thermal, photochemical and dimensional stability. As such, it has been widely used for laser and non-linear optical materials. The incorporation of Rhodamine B (RhB) (Figure 1) in the host polymer would obviously induce structural and morphological changes [62, 63]. Critical factors determining the optical response of a dye are related to the extent to which their physical and chemical properties are maintained. Thermal and optical properties of dye-doped polymers are important for the identification of suitable laser media. RhB is of great interest as it processes the highest photostability, ≈9,000 GJ mol^{-1} [64]. In this work, the electrospinning of PMMA–RhB nanofibers was performed, and the structure, morphology, and the linear and nonlinear optical properties of the resulting fibers were investigated.

Scintillating composites can find many potential applications due to their low cost and ease of preparation, high density and efficiency, size and compactness compared to other scintillation counters.

These composites could be used for a variety of applications which include gamma-ray spectroscopy, contamination surveys, land surveys and aerial radiological surveys for the presence of gamma- emitting radio nucleides. They can be used as detectors for safety detector requirements like in a scanner to rapidly identify a suspect luggage in a few cubic meter large container moving across the inspection device and remote detection of fissile materials These detectors can be used for laboratory applications, such as nuclear material processing, laboratory research activity, to field applications such as nuclear waste processing and management, nuclear explosion monitoring, maritime security and radioactive material transportation monitoring.
Scintillating composite fibers could find applications in medical imaging techniques, where a radioisotope is injected into the body, which produces ionizing radiation that can be detected by inserting a scintillating fiber sensor into the diseased part.

Scintillating fibers can also be used in the form of an array for imaging purposes in order to determine something about the physiology or anatomy of the target organ.

THEORETICAL PART

SCINTILATION MATERIALS

FUNDAMENTALS OF SCINTILLATION

The excitation of the electron is caused by absorption of energy from an external source such as another electron, a photon or an electric feld. An excited electron occupies a quantum state whose energy is above the minimum energy ground state. The mechanism of scintillation involves at least two steps: first the excitation of external energy and next the subsequent emission of photons. In the general, the activator absorbs directly the exciting radiation, which then raises it to an excited state. This excited state then returns to the ground state by the emission of radiation: a photon.

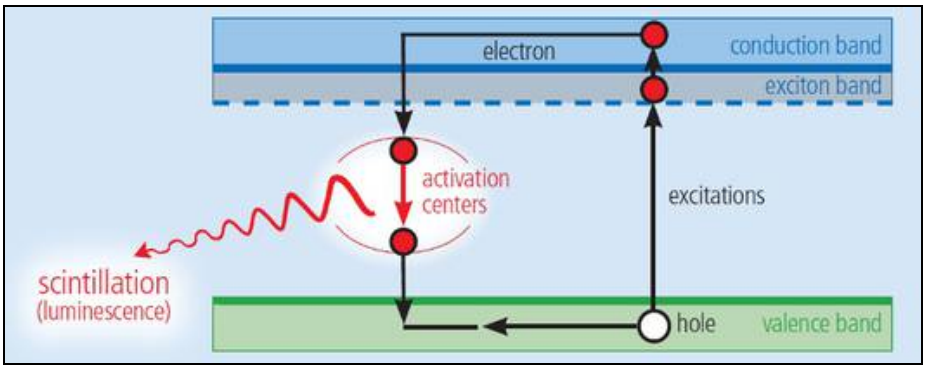

Figure 3 The principles of scintillation process

Absorption of incident radiation and creation of primary electrons and holes

When a charged particle hits a scintillating particle it dissipates its energy while passing through it. This energy transfer process takes place within 10^{-9} sec or probably less. The total energy from the high energy radiation maybe completely absorbed by the scintillating material or only a small portion may result in light emission. The gamma ray can transfer its energy to the scintillating material by the following process:

Photoelectric absorption- This happens at lower energies when the incident photon interacts with a tightly bound atomic electron. A photoelectron is produced from one of the electron shells (usually K-shell) of the absorber atom with energy a kinetic energy E_e

$$E_e = h\nu \qquad (1)$$

where $h\nu$ is the absorbed photon energy and E_e is the binding energy of the photoelectron in its original shell. When the photoelectron is ejected a vacancy is created in the atomic orbital, which is filled with an electron from a higher atomic orbit. This results in the emission of an X-ray, which might be absorbed in the material. If nothing escapes from the detector then the sum of the kinetic energies of the electrons equals the electrons that are created must equal the original energy of the incident gamma ray photon.

Compton Scattering- This process occurs at intermediate energies (0.5 to 3.5 MeV), when an incident ray scatters from a loosely bound electron in the absorbing material. This results in a recoil electron and scattered gamma ray photon. This photon is of longer wavelength and has less energy than the incident photon. The division of scattered energy and the wavelength shift is dependent on the scattering angle.

Pair production -This process occurs at higher energies where the incident γ-ray photon is used for production of mass of an electron-positron pair ($E= 2m_0c^2 =1.02$MeV where $m_0c^2 =0.52$MeV is the rest mass of the electron). If the incident γ-ray energy exceeds this value of E, then the excess energy appears in the form of residual energy shared between these electron- positron pair.

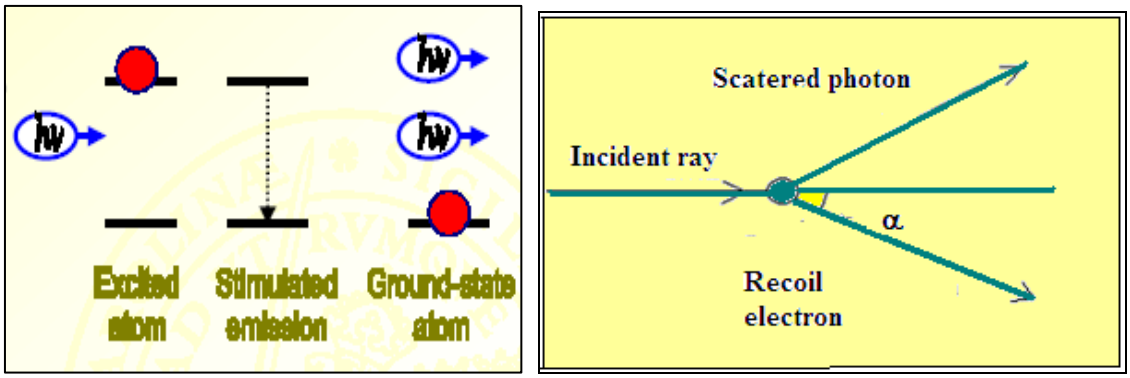

Figure 4 Compton scattering

The luminescent conversion of dissipated energy and emission of photons

An atom with an absorbed energy can be relaxed either by emitting a photon or by generating a secondary electron (Auger effect). Usually the probability of emitting photon decay is much greater that that of generation a secondary decay [67]. The energy might be dissipated in the ionization, excitation and possible dissociation of the molecules of the scintillating material. In a non-luminescent solid or liquid, the whole of this molecular energy is transferred into thermal, vibrational and translational energy and the molecules return to the ground state by radiationless transitions. Whereas in a scintillating material part of the excitation energy is re-emitted as photons of frequency υ_p, energy E_p $(=h\upsilon_p)$, wavelength λ_p $(=c/\upsilon_p)$ corresponding to direct energy transitions from an excited electronic level to the ground state. The photon emission is not spontaneous. The rate of photon emission decays exponentially with a decay period τ from its maximum intensity I_0.The intensity I after a time t is given by:

$$I=I_0 \exp(-t/\tau) \qquad (2)$$

The number of electrons emitted in the time interval t is:

$$p_t = p\,[1- \exp(-t/\tau)] \qquad (3)$$

Thus the relaxation of an atom with a hole occurs as a series of nonradiative and radiative transitions in a time of 10^{-13} to 10^{-15} secs.

Scintillators can be broadly classified as : 1) Inorganic and 2) Organic scintillators

INORGANIC SCINTILLATORS

These scintillators are used where high density and good energy resolution are required. They are characterized by a high stopping power due to their high atomic number, Z, which makes them most appropriate to detect high energy radiation. But they have longer decay times, in the order of hundreds of nanoseconds. There are three main classes of inorganic scintillators:

a) ***Activated scintillators***, such as NaI:Tl which has light output of 2.3 times that of anthracence, CsI: Na, CaF_2:Eu and $Lu_2SiO_{5:}Ce$, where the ionizing energy diffuses through the host crystal and produces an excited state at or near an activator atom that is present in low concentrations(typically~0.1%)

b) ***Self activated scitillators***, such as CsI, NaI, $Bi_4Ge_3O_{12}$, Bi_4SiO_{12}, BaF_2 and $PbWO_4$, where the activator atoms are a major constituent of the crystal and /or excitonic process are involved.

c) ***Core valence luminescence scitillators***, such as $BaF_{2,}CsF$ and $RbCaF_3$, where the ionizing radiation produces an electron vacancy in an upper core level of one atom and the vacancy use promptly (≈ 1ns) filled with an electron from the valence band of another atom to produce light [66].

The energy state of an inorganic scintillate material consists of a valence band, conduction band and forbidden band. When no energy is absorbed the lower valence band is completely filled with electrons bound at lattice sites. At room temperatures, there is some smearing of the energy distribution of the electrons, such that a small, but not insignificant number have enough energy to cross the energy band gap into the conduction band. The intermediate forbidden band consists of no electrons. These bands extend throughout the crystal and hence the scintillation depends on the crystal lattice of the material.

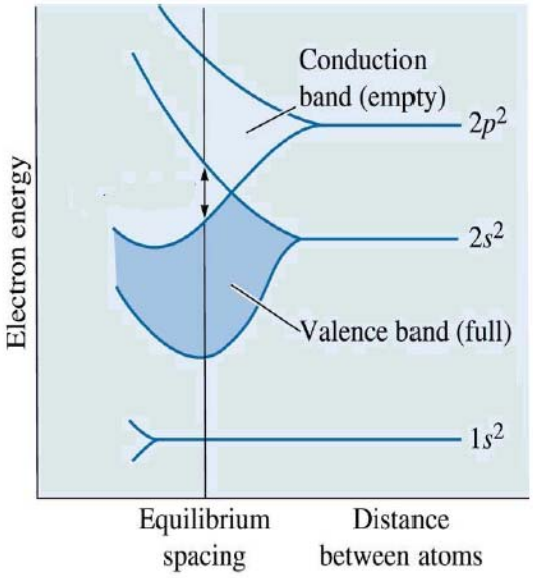

Figure 5. Scheme of energy bands in atom

When the scintillator absorbs radiation energy the electrons are excited and elevate to the conduction band from the valence band, creating holes in the valence band. The electrons falling back to valence band emit high-energy photon, which would lie beyond the visible region for a pure crystal. This band gap needs to be reduced in order to lower the energy of the emitted photon to the visible range. When small amount of impurity called activators are added to the inorganic scintillator, it creates energy states within the forbidden band through which the electron can de-excite back to the valence band, thus increasing the probability of visible photon emission during de-excitation.

When ionizing radiation strikes the scintillate material, it excites an electron out of its energy level consequently leave a hole and creating electron-hole pairs. These holes which act like positive charge drift towards an activator site and ionize it. A positive electric charge is produced when an electron bound to an atom or molecule absorbs enough energy from an external source to escape from the electric potential barrier that originally confined it. This happens because the ionization energy of the activator is less than the positive hole. When a free electron migrates towards an ionized activator it forms a neutral state having its own energy states. Now, the scintillation occurs through

the de-excitation of the activators to the ground state by the emission of photons. This transition will occur in the visible range with the half lives being in the order of 10^{-7} s.

There is possibility of quenching mechanism taking place when the electron gets trapped in the activator site and the de-excitation to the ground state produces radiationless transitions or no visible photons.

A third possibility exists when an electron reaches a metastable state and may jump back to the conduction band acquiring thermal energy from the lattice vibrations and then de-excite to the ground state giving rise to a slow component of light called phosphorescence [67- 69].

ORGANIC SCINTILLATORS

a) ***Organic Crystalline Scintillators-*** These are organic molecules, which have an aromatic ring. They are characterized by a fast response, in the order of one nanosecond. When pure, they form crystals, which are difficult to shape.

Anthracene is one of the best known organic scintillator with good energy resolution and maximum quantum efficiency of 90%. Napthalene is an organic scintillator whose relative response to different ionizing particles is similar to that of Anthracene [67]. Stilbene is a crystal scintillator with high scintillation efficiency and short scintillation decay time. In organic scintillators light emission occurs as a result of fluorescence where the molecule gets excited by energy absorption from ionizing radiation particles. The scintillation response of organic phosphors to heavy particles is less compared to electrons of equal energy. Here the fluorescence excitation by ionizing particles is less compared to photo-excitation since much of the energy of incident particle is dissipated as heat [67- 69].

The manner in which particle energy is dissipated as ionization and excitation in a scintillator appears as visible light is essentially different in organic, as compared to inorganic materials. When the scintillating material absorbs the radiation energy, the high-energy particles or photons collide with the electrons in the material. The electrons become excited and jump to higher energy states. Since the electrons in the excited state have the same spin as they did in the ground state, they are not stable and almost

spontaneously become de-excited to lower energy levels, releasing energy in the form of light. This phenomenon is known as fluorescence, which is an “allowed” transition. When the excited state is meta-stable then light emission continues even after the source of energy is removed. These excited states give rise to electron transitions to lower energy states resulting in phosphorescence. Here the direct transition to the ground state is “forbidden” [68, 69].

Fluorescence

As shown in the Figure 2.5, the organic molecules have symmetric properties related to π – electron structure, where regions 1 and 2 represent absorption, 3 fluorescence, 4 inter-system crossing and 5 phosphorescence. A series of singlet state with spin 0 are shown as $S_{0,}$ $S_{1,}$ $S_{2...}$ a series of triplet state with spin 1 as $T_{1,}$ T_{2}, T_{3} .…

These electronic configurations are further subdivided into levels with smaller spacing such as S_{00}, S_{01}, S_{02} and so on corresponding to vibrational state of the molecules. The lowest vibrational state of the ground electronic state is represented by $S_{00.}$

Before the excitation of electrons, they are in the lowest vibrational level of the ground electronic state. Absorbing the kinetic energy of the charged particle excites the

electrons, allowing them to enter a higher vibrational level in the excited state. The electrons in higher singlet excited states are quickly de-excited to the S_{1} electron state through radiationless transfer or quenching. Any higher state such as $S_{11,}$ S_{22} in not in thermal equilibrium with its neighbors and again loses that vibrational energy.

The electrons in the excited state have the same spin as they did in the ground state. The electrons in S_{10} state jump back to the ground state, re-entering it first at a higher vibrational level before losing the excess vibrational energy in the form of scintillating light.

The wavelength of light absorbed for excitation will be shorter than the wavelength emitted during de-excitation. (Stokes' law). The fluorescence decays exponentially with a decay time τ and the intensity I after a time t is given by:

$$I = I_0 e^{-t/\tau} \qquad (4)$$

This fluorescent state can exist for a few nanoseconds [67-69].

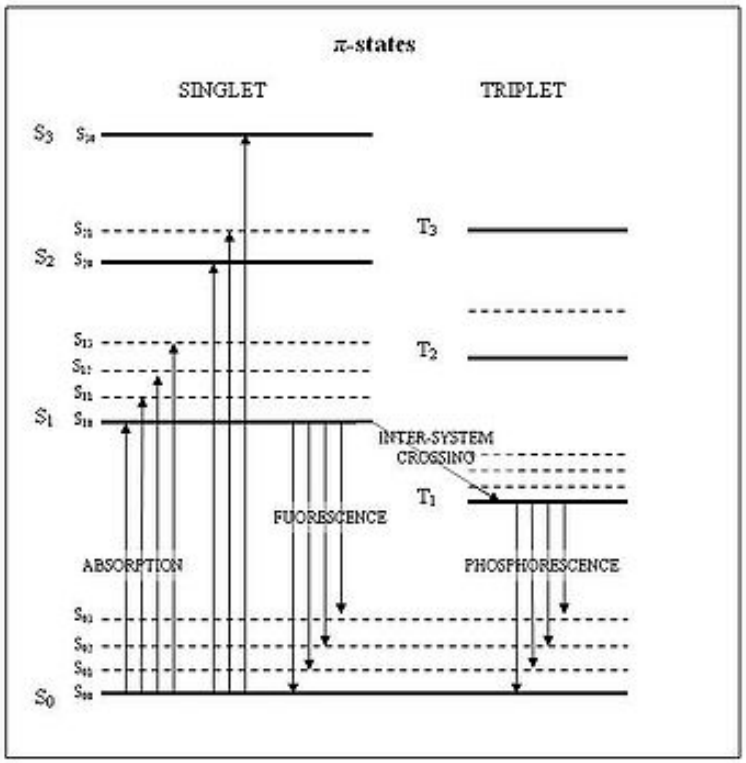

Figure 6 The π-electron structure of organic scintillators showing the energy levels

Phosphorescence

In this process light emitted by an atom or molecule persists after the exciting source is removed. While excited, the electrons experience a change in spin called intersystem crossing where some excited singlet states may be converted to triplet states. This change in spin places the electrons in a metastable position forbidding them to move back into the ground state. Thermal energy from within the crystal structure releases the electron from the troughs, which causes them to be raised to a higher, less stable energy level where they can eventually fall back to lower energy levels. During this de-excitation from T_1 to S_0 there is delayed light emission known as phosphorescence.

Phosphorescent states can exist from 10^{-4} seconds to several hours and wavelength maybe longer than that of fluorescence spectrum.

We thus see that scintillation in organic materials is inherently a molecular property and is exhibited in liquid and solid solutions, and in the solid, liquid, vapor, plastic and glassy states [67-69].

ELECTRONIC AND OPTICAL PROPERTIES OF $Bi_{12}SiO_{20}$ (BSO) SCINTILLATORS

Electronic and crystal structure of BSO

Bismuth silicon oxide, (BSO), belongs to the sillenite family, with the general formula $Bi_{12}MO_{20}$ (M = Si, Ge, Ti, Pb, Mn, B1/2P1/2). Lars Gunar Sillen uncovered $Bi_{12}SiO_{20}$ 1941, in Durango, Mexico and latter the whole group was named after him. BSO is considered to be a promising material in LTCC technology, because of its piezoelectric, electro-optic, photo-refractive and optically active properties [71]. BSO is a stoichiometric sillenite with a fully occupied oxygen sublattice that meets all the major criteria for application in LTCC modules, such as a low sintering temperature (TS = 850 8C) as well as a chemical compatibility with metal electrodes and other functional ceramics [70]. The dielectric properties of BSO include low dielectric losses and a sufficiently suppressed temperature coefficient of resonant frequency tf [70]. The bismuth ortho-germanate Bi4Ge3O12 (BGO) and bismuth ortho-silicate Bi4Si3O12 (BSO) are technologically important materials owing to their remarkable characteristics such as fast luminescent decay constant, large light output and radiation hardness [70]. Both are used as high-efficient scintillators in gamma ray spectroscopy and high energy physics, and widely applied in non-linear optical devices and nuclear medicine (X-ray and positron computer tomography) [71].

All compounds with the $Bi_{12}MO_{20}$ structure crystallize in the cubic system with I23 space group [70], figure 7.

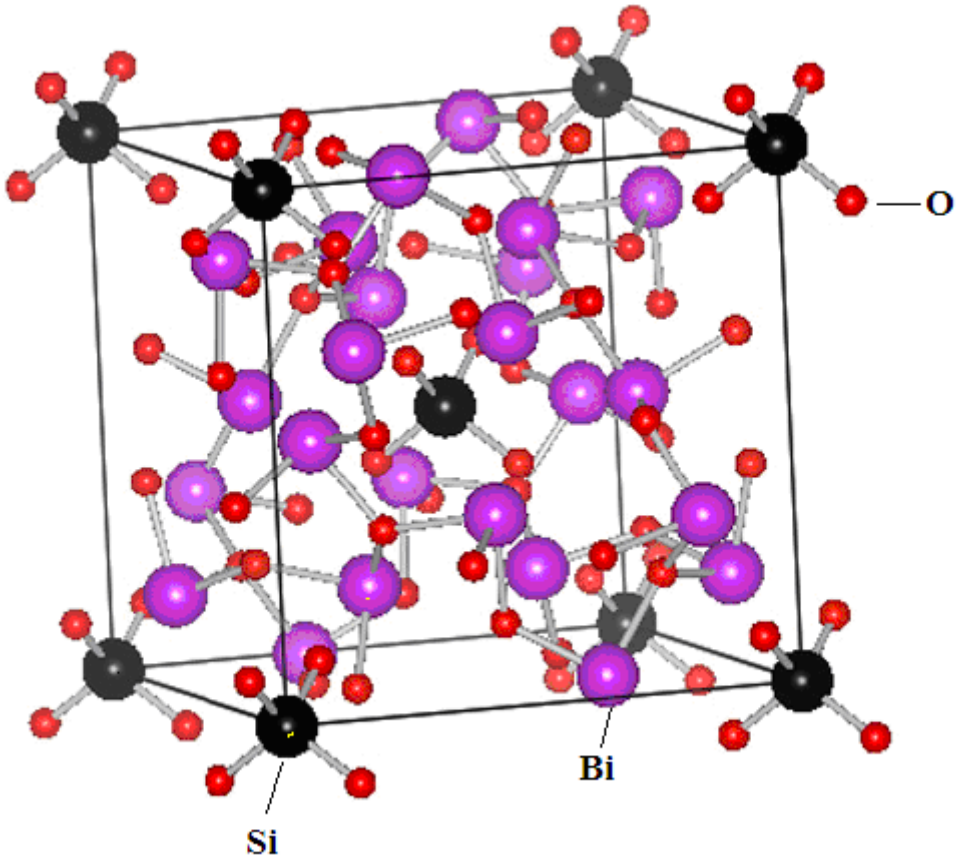

Figure 7 Crystal unit of BSO [70]

Figure 8 illustrates the diffuse reflection spectra (DRS) and the absorption spectra of the as-prepared Bi12SiO20 powders in comparison with P25 TiO2. The absorption spectra is transformed from the DRS according to the Kubelka–Munk theory [70]. It can been seen in Figure 8 that the $Bi_{12}SiO20$ powders can absorb visible light in the wavelength range 400–550 nm, which is in agreement with the pale yellow color of the synthesized sample. Bi12SiO20 crystal is a semiconductor with an indirect band gap [71]. Therefore, plots of (hva)1/2 versus hv should be linear in the vicinity of absorption edge, and the intercept with hv-axis yields the forbidden band gap, Eg. The (hva)1/2 curve as a function of hv for Bi12SiO20 powders. The calculated Eg of Bi12SiO20 powders is 2.80 eV, which is fairly consistent with the reported 2.60 eV for the bulk single crystal $Bi_{12}SiO_{20}$ [71].

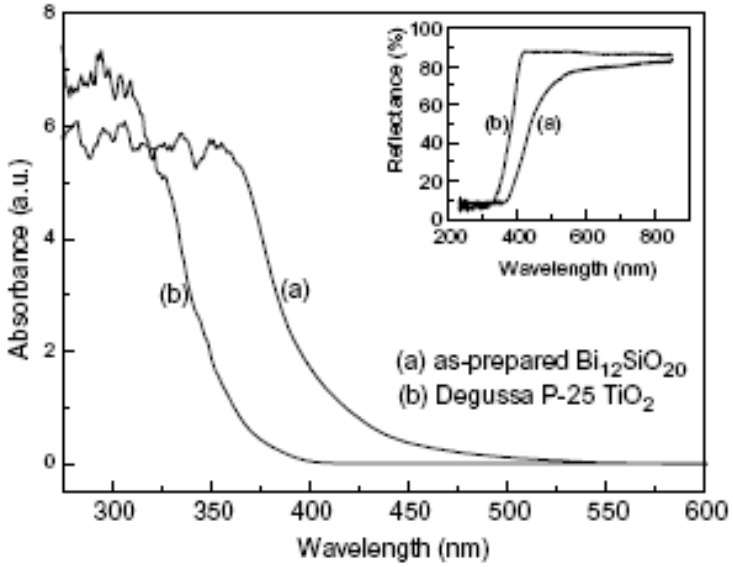

Figure 8 Absorption and UV–Vis of $Bi_{12}SiO_{20}$ powders [71].

Optical properties

The results of the FP-LAPW calculations for the imaginary part of ε for BSO are presented in Fig. 9.

The calculated spectra can not be directly compared with the experimental ones since the latter refer to absorption of radiation wavelengths greater than 300 nm, caused by electronic transitions to the impurity or exciton levels within the band gap of the compounds. The calculated optical spectra were, however, shifted in energy in order to fit the experimentally determined band gaps in BSO. A quick look at the Fig. 9 reveals that the BGO absorbs mostly in the region between 160 and 300 nm, while the region of the principal absorption of the BSO is much narrower: between 160 and 230 nm. These are the wavelengths by which the materials should be optically excited. A fact that the BGO absorption is efficient in the wider range of the wavelengths makes him favorable in comparison with the BSO. The analysis of the absorption spectra in Fig. 9 reveals the manner in which the incident radiation is absorbed in the materials. It is not the Bi atom that takes the radiation energy (Bi-s to Bi-p absorption is negligible). The O atoms around the Bi absorb the energy (p-electrons) and transfer it to the Bi p-electrons. By this way, the luminescent center in BGO and BSO, which is the Bi, receives the energy which turns him to the excited state. The process of emission of

light, which occurs when the Bi returns to its ground state, can not be analyzed by present theory since it does not describe adequately the excited states of the system. Knowing the complex dielectric tensor e one can calculate various optical constants which characterize the propagation of the electromagnetic wave through the material. One of the most important is the complex refractive index, defined as:

$$N(x) = n(x) + ik(x) \qquad (5)$$

where *n* and *k* are the refractive index and extinction coefficient, respectively. The knowledge of n provides various useful information about the optical properties of the material. The extinction coefficient *k* directly describes the attenuation of the electromagnetic waves within the material, and is also known as a damping constant or attenuation coefficient. The relation between the n and k and the dielectric function e is written as: Re(e) = n2+k2; Im(e) = 2nk. Fig. 9 displays the variation of the refractive index, extinction coefficient and the reflectivity of BSO as a function of the energy of incident radiation, as calculated by the FP-LAPW method.

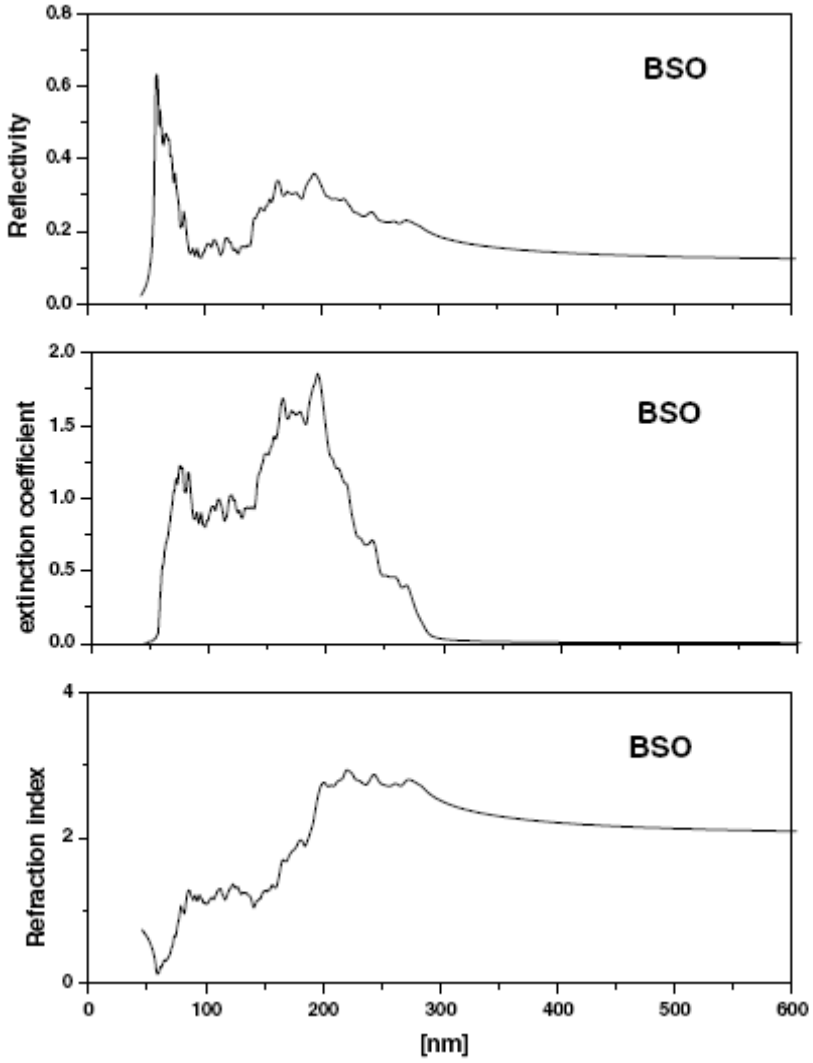

Figure 9 The extinction coefficient, the reflection and refraction indexes for the BSO compound [70]

POLYMER COMPOSITES WITH INORGANIC SCINTILLATORS

Composites with polymer matrix with embedded inorganic scintillate particles have been investigated in optoelectronics. Experiment shows that all the attempts to introduce heavy inorganic scintillating powders of BaF2; CeF3; CsI; BGO, BSO etc. in polymer matrix resulted in the occurrence of composite materials with small attenuation lengths, which are useless in particle detectors. The reasons for such low transparency

occurrence showed that to obtain an optimal level of transparency, it is necessary to fulfill the following conditions: a) the refractive indices of plastic matrix n_p and introduced crystals n_c should be as close to each other as possible [11]; that is, the optical contrast should be $n_p / n_c \cong 1$; b) the achievement of good mechanical and optical properties requires the provision of good adhesion, or even the creation of chemical bonds, at the boundary between dissimilar components in composite materials; c) in order to prevent unnecessary loss of transparency, small crystals should not have fine fractions; that is, the size of introduced crystals should be as large as possible; d) the best shape of the introduced crystals to achieve the maximum level of transparency and density is a small crystal ball; e) in order to secure light output uniformity, the light outputs of its components should be similar; f) in order to keep the radiation resistance at the maximum level, the radiation resistance of the introduced crystals should not be lower than the radiation resistance of its plastic matrix.

Fluorescence resonance energy transfer properties of photo luminescent-dye doped polymer

The optical excitation of a molecule and its subsequent emission of spontaneous luminescence or stimulated radiation results in a series of intermolecular processes, such as orientation or translational, which occur in both the ground and excited states.1 The orientation relaxation processes have a substantial effect not only on the spontaneous luminescence spectrum but also on the stimulated emission spectrum of the solution.

Rhodamine dyes are used as the active medium of tunable laser radiation in the visible region of the light spectrum. They appear red to violet in color. The molecular formula of Rhodamine B (RB) is $C_{28}H_{31}ClN_2O_3$ with molecular weight of 479.02 gm/mol (Figure 10). It is often used as a tracer dye in water to determine the rate and direction of flow and transport. Rhodamine dyes are used extensively in biotechnology applications such as fluorescence microscopy, flow cytometry, fluorescence c correlation spectroscopy and ELISA.8 RB is tunable around 610 nm when used as a laser dye. Its luminescence quantum yield is 0.65 in basic ethanol, 0.49 in ethanol and 1.012 and 0.68 in 94% ethanol. The fluorescence yield is temperature dependent.

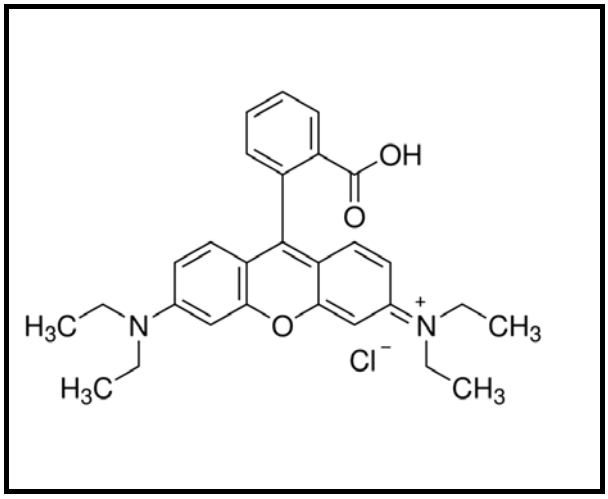

Figure 10 Structure formula of Rhodamine B

Organic dye molecules have been widely used in solutions as amplifying media in tunable lasers. However, there are various advantages of trapping them in solid host such as, no need of using volatile/toxic solvents and cumbersome system design. The possibility of trapping these molecules in solid matrix leads to new field of applications of these lasers. The common goals for developing solid state dye lasers are high power, high efciency, superior reliability, compactness and environmental safety. There are various factors which a!ect the laser performance of solid-state dye lasers. Factors such as dye concentration, thickness of the active region, photophysical limits of the samples, and pumping parameters/geometry, etc., a!ect the overall performance. Recently, it was pointed out the importance of sample dye concentration in lasing performance of rhodamines in HEMA/MMA copolymers. There are some reports of using modifed polymethylmethacrylate (PMMA) as host material either by adding low molecular weight compound to PMMA or by copolymerizing it with other polymers. Although lasing properties of dyes in PMMA have been studied to a large extent, the understanding of lasing performance of various laser dyes and its correlation to photophysical properties in PMMA is not satisfactory. Proper understanding of these properties helps in leading to new applications of these materials.

In the case of the organic-dye impregnated nanocomposites, the nanoconfined organic dyes might undergo an energy transfer, resulting in the enhancement of the fluorescent signal at low dye concentrations. [72, 73] Wang and Tan fabricated silica nanoparticles

encapsulated by three organic dyes. They suggested that the fluorescence resonance energy transfer (FRET)-mediated emission characteristics could be tuned using single wavelength excitation by varying the doping ratio of the three tandem dyes.[73] Most investigations related to energy transfer have been conducted using chromophore embedded thin films due to the distance-dependent character of the energy transfer between the donor and the acceptor.[74] In addition, chromophores confined to nanometer dimensions, such as micelles, mesoporous silica or carbon, and zeolites, have also been investigated concerning the energy-transfer system.[75] Organic-dye embedded polymer nanocomposites have attracted much attention because of their biocompatibility, facile preparation, and diverse functionality.[76,77]. Having demonstrated the feasibility of this technique for FRET applications, it was prompted to embed photoluminescent dyes, such as coumarin 6 (Cm6) and rhodamine B (RhB), into poly(methyl methacrylate) (PMMA) and observed the FRET properties in this system. The overall synthetic procedure of organic-dye embedded PMMA nanofibers is illustrated in Scheme 1. At first, the PMMA nanotubes with uniform wall thickness were fabricated using VDP. The PMMA nanotubes impregnated in the AAO membrane provided the inner wall on which the organic dyes with selective concentration were loaded. Additional VDP was carried out to encapsulate the organic dyes.The other method is Electrospinning.

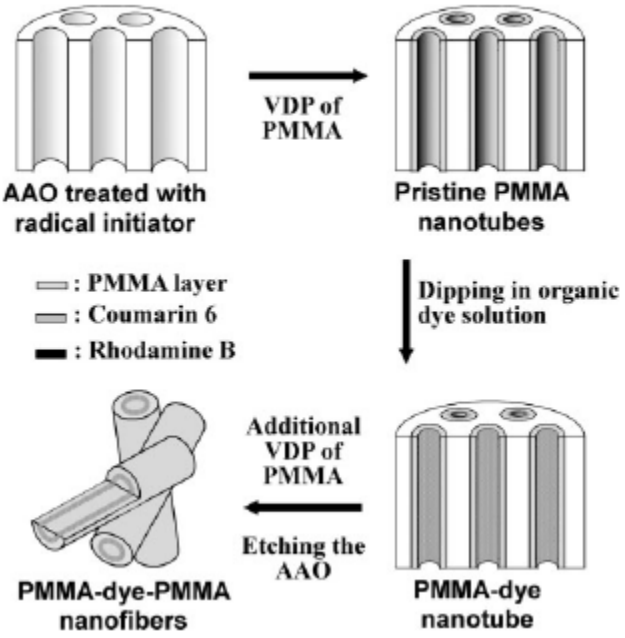

Figure 11 Schematic diagram of the fabrication of PMMA nanotubes and PMMA–dye–PMMA nanofibers. [78]

ELECTROSPINNING

Electrospinning is a unique process to produce submicron polymeric fibers in the average diameter range of 100 nm-5 μm.1-4 Fibers produced by this approach are at least one or two orders of magnitude smaller in diameter than those produced by conventional fiber production methods like melt or solution spinning.5 In a typical electrospinning process (Figure 11), described extensively in the literature,6-10 a jet is ejected from the surface of a charged polymer solution when the applied electric field strength (and consequently the electrostatic repulsion on the surface of the fluid) overcomes the surface tension. The ejected jet travels rapidly to the collector target located at some distance from the charged polymer solution under the influence of the electric field and becomes collected in the form of a solid polymer filament as the jet dries. During its flight to the target, the jet undergoes a series of electrically driven bending instabilities that gives rise to a series of looping and spiraling motions. In order to minimize the instability caused by the repulsive electrostatic charges, the jet

elongates to undergo large amounts of plastic stretching that consequently leads to a significant reduction in its diameter. However, the degree of molecular orientation in a fiber spun from a solution of an amorphous polymer is not generally high. This is due to the high molecular mobility in fibers containing solvents (chain relaxation is often faster than the time it takes for the solvent to evaporate completely from the fiber).

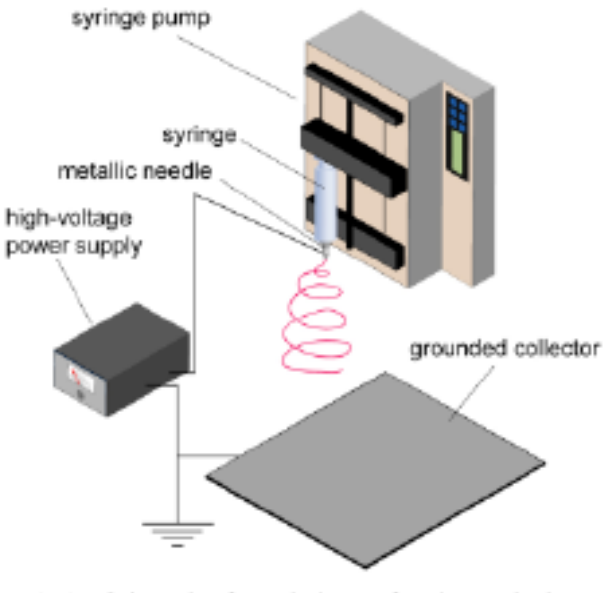

Figure 12 Schematic of the electrospinning apparatus utilized to electrospin PMMA

solutions [79]

Current research efforts have focused in understanding the formation, shape, texture and morphology of electrospun fibers. In fact, the principal parameters that affect fiber diameter are as follows: *system parameters* – viscosity, net charge density (conductivity), surface tension of the polymer fluid, molecular weight, molecular weight distribution and topology (branched, linear etc.) of the polymer; *process parameters* - electric field strength (electric potential and tip-target separation distance), flow rate of the polymer solution, concentration, ambient parameters (temperature, humidity and air velocity in the electrospinning chamber), internal diameter of the nozzle/capillary, and motion of the target substrate. In the past, the effect of various parameters, particularly

viscosity and surface tension, on fiber diameter has been investigated. It has also been observed that increasing the concentration (and consequently viscosity) while lowering the surface tension favors the formation of bead-free and uniform fibers. A direct correlation has been observed between *uniform* fiber diameter and solution viscosity,, however, more detailed investigations on the dependence of fiber formation and fiber morphology on molecular weight (MW), molecular weight distribution (MWD), topology and solution rheology need to be done. The effect of solution rheological behavior on fiber morphology of linear and branched copolymers (11,700-106,00 g/mol M_w) of poly(ethylene terephthalate-co-ethylene isopthalate) (PET-co-PEI) that were electrospun from a good solvent combination of 70/30 w/w mixture of chloroform and *N,N*-dimethyl formamide ($CHCl_3$/DMF). In that study, investigation of the dependence of electrospun fiber diameter on concentration in the semidilute entangled and concentrated regime was made, in addition to investigating correlations between viscosity and concentration in different concentration regimes. A systematic approach to investigate electrospun *fiber formation* in different concentration regimes (dilute, semidilute unentangled and semidilute entangled) is very relevant to understand the process of fiber formation from a solution rheological standpoint and the effect it has on electrospinning. While some of these issues were addressed in the previous study[33], the present study aims to further investigate and test the effects of scaling relationships between viscosity and concentration in different concentration regimes *on fiber formation and morphological features of electrospun systems.* This was done by utilizing a series that covers a relatively wider range in molecular weight, viz. 12,470 g/mol to 365,700 g/mol weight average (M_w) as compared to that utilized in the earlier study. In addition, *narrow (M_w/M_n~1.03-1.35) and relatively broader* (*M_w/M_n~1.62-2.12*) MWD linear homopolymers of poly(methylmethacrylate) (PMMA) were utilized in the present investigation. Electrospinning of all solutions in a good solvent, *N,N*-dimethyl formamide (DMF), was conducted at identical processing conditions.

Photonic structures with wavelength-scale dimensions offer interesting opportunities to engineer the optical properties of embedded emitters, which depend strongly on the surrounding of the light emitters [80, 81]. Particularly, for dimensions approaching the wavelength of light, the associated strong modification of the local photonic density of states alters the photophysical properties of the emitters. Similarly, fluorophores

deposited on surfaces [82], placed close to a metallic mirror [83, 84] or embedded in dielectric particles [85] were shown to display different radiative decay rate, quantum yield and photobleaching rate. Besides the size of the structures also the position of the light emitter within the structures and the orientation of the emission dipole moment with respect to the interfaces (electromagnetic boundaries) play a substantial role [86, 87]. We show here how electrospinning is used to prepare hybrid, luminescent nanofibers. Fluorescent molecules and luminescent semiconductor nanoparticles (quantum dots) are embedded into fibers with diameters ranging from 50 nm to several micrometers. We show the influence of the fiber diameter on the single molecule fluorescence lifetime (τ_f) distributions of the embedded chromophores. For diameters of fibers below 500 nm a significant broadening of τ_f distributions is observed.

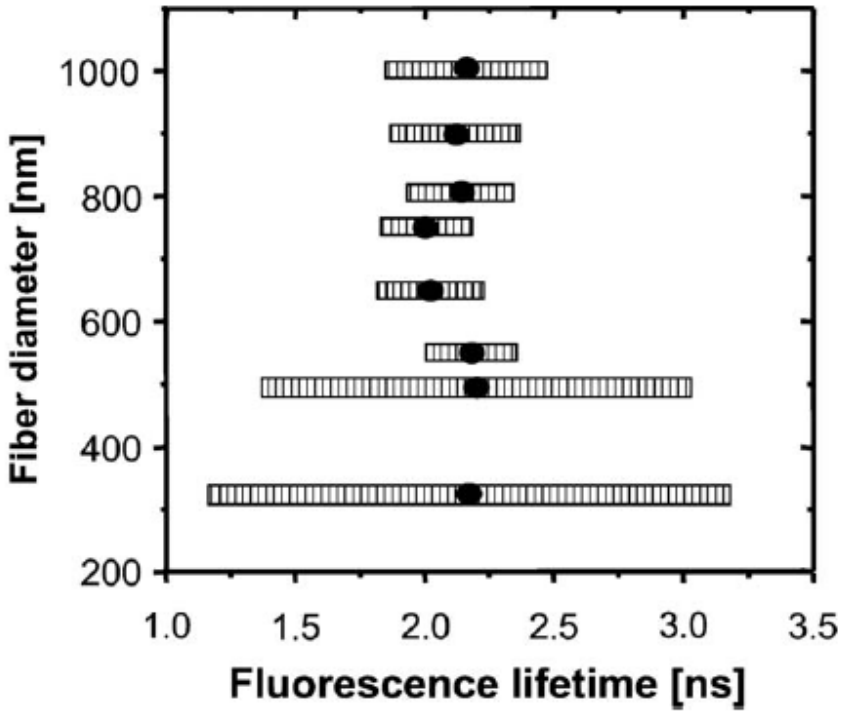

Figure 13 Mean values of sf distributions as a function of fiber diameter [40].

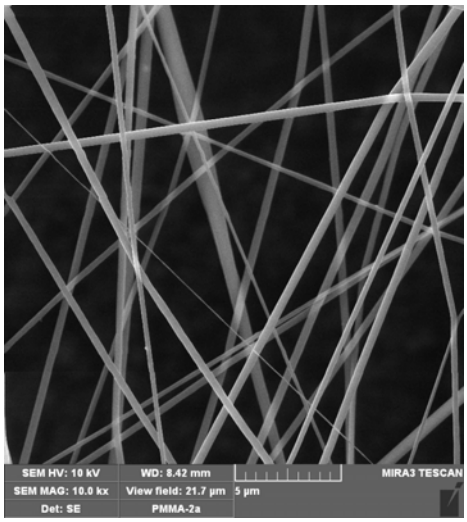

a)

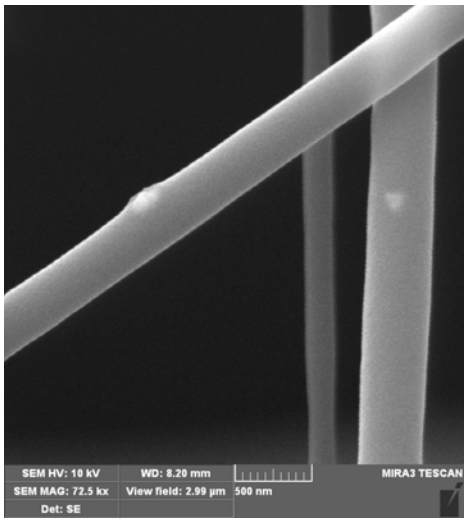

b)

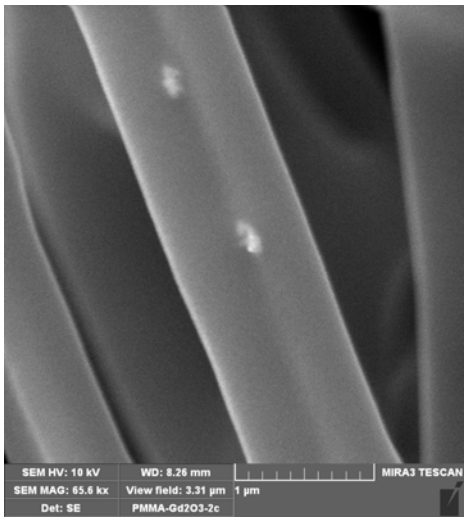

c)

Figure 14 Electrospun nanofibers of a) PMMA; b) and c) nanocomposite nanofibers PMMA with Gd_2O_3 (Eu^{3+})

CHARACTERIZATION OF SCINTILATING COMPOSITES WITH POLYMER MATRIX

STRUCTURE AND MORPHOLOGY

X-Ray Diffraction (XRD)

X-ray diffraction is a nondestructive technique, and is one of the widely used for determining lattice parameters, preferred orientation of the crystal, phase composition (qualitatively and quantitatively), grain sizes, lattice strain, residual stress etc. XRD can provide the information from a relative lager area of the specimen compared to TEM. When a monochromatic x-ray beam incident onto a crystal sample, the constructive diffractions (or interference) from parallel planes of atoms with inter-planar spacing d occur if Bragg's law is satisfied (figure 18) [71]:

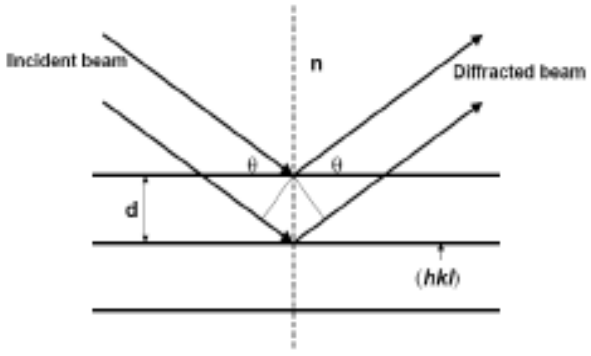

Figure 15 Schematic diagram of Brag's diffraction from a set of parallel planes

$$2d\sin\theta = n\lambda \qquad (6)$$

where ***n*** is integer that indicates the order of the reflection, θ is Bragg angle, and λ is the wave length of the x-ray beam. Figure 13 Schematic diagram of Bragg's diffraction from a set of parallel planes. By measuring the Bragg angle θ, the interplanar distant ***d*** can be obtained if the wavelength of the x-ray beam is known [72]. Furthermore, the lattice parameters are related with Miller indexes (***hkl***) of each reflection plane and interplanar distance (***dhkl***). For example for hexagonal and cubic structures, we have, respectively:

$$\frac{1}{d_{hkl}^2} = \frac{4}{3}\left(\frac{h^2 + hk + k^2}{a^2}\right) + \frac{l^2}{c^2} \tag{7}$$

$$a = d_{hkl}\sqrt{h^2 + k^2 + l^2} \tag{8}$$

On the other hand, the first treatment of particle size broadening was done by Scherrer. By making some simplifications, e.g., taking a powder sample of a small cubic crystal, and assuming they are free from strains and faulting, so that the peak broadening is due only to the small size, the following Scherrer's equation [71]

$$D = \frac{K\lambda}{B\cos\theta} \tag{9}$$

where D is the particle diameter, θ is the diffraction angle, and B is the full width at the half high maximum (FWHM). The factor K involves different instrumental aspects, such as geometry, penetration of X-Ray in the sample, etc. From the width of the diffraction peak using the Scherrer's equation, one can calculate the average particle size. However, the width of diffraction peaks is broadening due to presence of defects or strain in the crystal lattice. The extreme case corresponds to amorphous materials, for

which the peaks disappear totally. In nanostructured materials, the Scherrer's equation provides an estimated value of the crystal size.

Scanning electron microscopy (SEM)

According of formation of imaging and resolution, most microscopes can be classified as one of three basic types: optical, charged particle (electron and ion), or scanning probe. Optical microscopes are the ones most familiar to everyone from the high school science lab or the doctor's office. They use visible light and transparent lenses to see objects as small as about one micrometer (one millionth of a meter), such as a red blood cell (7 μm) or a human hair (100 μm). Electron and ion microscopes, the topic of this booklet, use a beam of charged particles instead of light, and use electromagnetic or electrostatic lenses to focus the particles. They can see features as small a tenth of a nanometer (one ten billionth of a meter), such as individual atoms. Scanning probe icroscopes use a physical probe (a very small, very sharp needle) which scan over the sample in contact or near-contact with the surface. They map various forces and interactions that occur between the probe and the sample to create an image. These instruments too are capable of atomic scale resolution.

The main components of a typical SEM are electron column, scanning system, detector(s), display, vacuum system and electronics controls (fig. 16). The electron column of the SEM consists of an electron gun and two or more electromagnetic lenses operating in vacuum. The electron gun generates free electrons and accelerates these electrons to energies in the range 1-40 keV in the SEM. The purpose of the electron lenses is to create a small, focused electron probe on the specimen. Most SEMs can generate an electron beam at the specimen surface with spot size less than 10 nm in diameter while still carrying sufficient current to form acceptableimage. In order to produce images the electron beam is focused into a fine probe, which is scanned across the surface of the specimen with the help of scanning coils (fig. 17). Each point on the specimen that is struck by the accelerated electrons emits signal in the form of electromagnetic radiation. Selected portions of this radiation, usually secondary (SE) and/or backscattered electrons (BSE), are collected by a detector and the resulting signal is amplified and displayed on a TV screen or computer monitor. The resulting

image is generally straightforward to interpret, at least for topographic imaging of objects at low magnifications.

The electron beam interacts with the specimen to a depth approximately 1 μm. Complex interactions of the beam electrons with the atoms of the specimen produce wide variety of radiation. The need of understanding of the process of image formation for eliable interpretation of images arises in special situations and mostly in the case of high magnification imaging. In such case knowledge of electron optics, beam-specimen interactions, detection, and visualization processes is necessary for successful utilization of the power of the SEM.

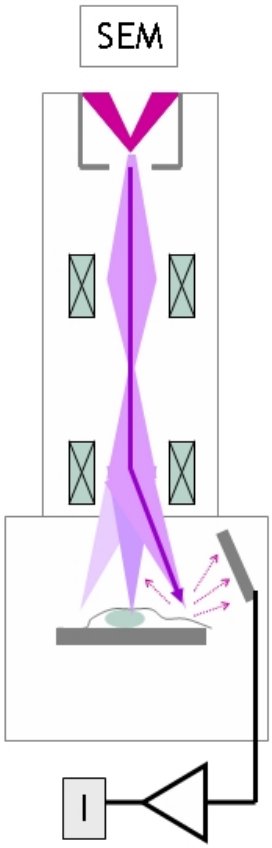

Figure 16 Scheme of forming imaging of SEM

MECHANICAL PROPERTIES

Nanoindentation- determining the elastic modulus and hardness

Hardness has conventionally been defined as the resistance of a material to permanent penetration by another harder material with measurement being made after the test force has been removed, such that elastic deformation is ignored. Instrumented indentation hardness provides the ability to measure the indenter penetration h under the applied force F throughout the testing cycle and is therefore capable of measuring both the plastic and elastic deformation of the material under test. Figure 16 is a typical load displacement hysteresis curve obtained from an elastic / plastic material and Figure 17 shows the schematic representation of the indent under load and in the unloaded condition. Apart from the measurement of the indenter penetration under the applied force, the unloading contact compliance C (= 1/S) and the contact depth hc can be calculated. The value of hc is dependent on the exact shape of the indenter and material response to the indentation; 'sinking-in' and 'piling-up' around the indenter also affect the value.

Since 1992, the analysis method proposed by Oliver and Pharr [88] has been established as the standard procedure for determining the hardness and elastic modulus from the indentation load-displacement curves for bulk materials. In the Oliver-Pharr method, the projected contact area between indenter tip and material is estimated using the equations for the elastic contact of an indenter of arbitrary shape on a uniform and isotropic half space. The indentation modulus and hardness of the material can thus be calculated without the necessity of imaging the indentation after the experiment. The Oliver-Pharr method was initially developed for analyzing indentations in bulk materials, not for films on substrates, and no information about a possible substrate is included in the analysis. The Oliver-Pharr method is, however, frequently used by researchers to interpret indentations performed on thin films in an attempt to obtain approximate film properties regardless of the effect of substrate properties on the measurement.

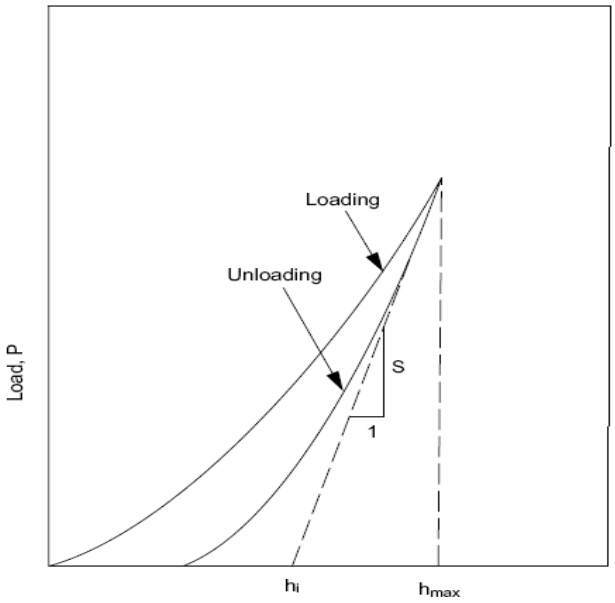

Figure 17 Typical force displacement curve showing measured and derived parameters [88]

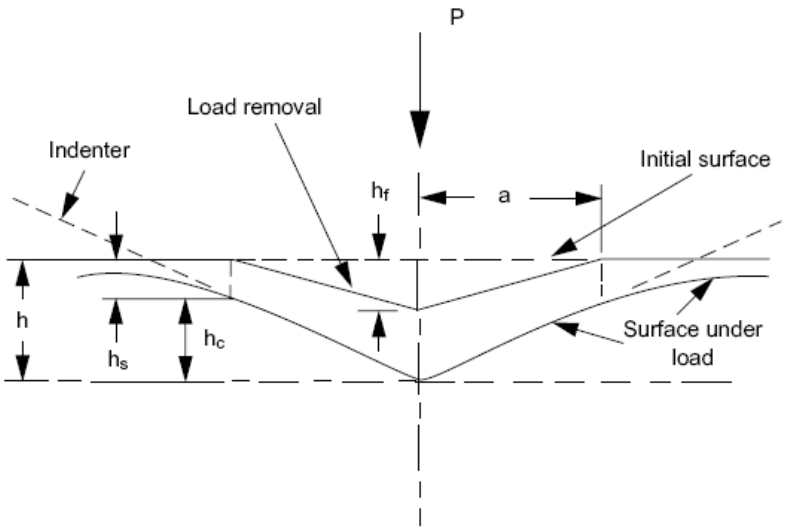

Figure 18 Schematic of indentation showing the displacements observed during an indentation experiment [88]

A schematic representation of a typical load versus indenter displacement data for an indentation experiment is shown in Figure14. For the analysis of the loaddisplacement curve we make the following assumptions]:

a. Deformation upon unloading is purely elastic.
b. The compliances of the specimen and the indenter tip can be combined as springs in series.
c. The contact can be modeled using the analytical model developed by Sneddon for the indentation of an elastic half space by a punch that can be described by an axisymmetric solid of revolution.

According to assumption b) the effect of a non-rigid indenter on the load-displacement curve can be accounted for by defining a reduced modulus, *Er*, by

$$\frac{1}{E_r} = \frac{1-\nu}{E} + \frac{1-\nu_i^2}{E_i} \tag{10}$$

where E and ν areYoung's modulus and Poisson's ratio for the specimen and E_i and ν_i are the same quantities for the indenter.

A cross section of an indentation is shown in Figure 14b). During loading the total displacement h is written as

$$h = h_c + h_s \tag{11}$$

where h is the vertical distance along which contact is made (called contact depth), h_s is the vertical displacement of the surface at the perimeter of the contact and h_c is the penetration depth of the indenter under load. When the indenter is withdrawn the final depth of the residual hardness impression under load is h_f . The determination of Young'smodulus is based on Hertz contact equation according to which

$$E_r = \frac{\sqrt{\pi}}{2}\frac{S}{\sqrt{A}} \tag{12}$$

where A is the contact area and S is the stiffness of the unloading curve $(S = dP/dh)$. According to Oliver and Pharr the unloading data for stiffness measurement are fitted into equation

$$P = B\left(h - h_f\right)^m \tag{13}$$

where P is the load, $(h - h_f)$ is the elastic displacement and B and m are material constants. The quantities B, m and h_f are determined by a least squares fitting procedure of the unloading curve. For the analysis it is assumed that the geometry of the indenter is described by an area function $A = A(h)$ which relates the cross-sectional area of the indenter to the distance from its tip. The contact area at maximum load is given by

$$A = A\left(h_c\right) \tag{14}$$

The contact depth at maximum load, hc, that is, the depth along the indenter axis to which the indenter is in contact with the specimen, is determined by

$$h_c - h_{max} - \varepsilon\left(h_{max} - h_i\right) \tag{15}$$

where h_{max} is the maximum depth and h_i is the intercept depth, that is, the intercept of the tangent to the unloading load-displacement curve at maximum load with the depth axis. The constant ε is a function of the shape of the indenter tip. It takes the value 1 for a flat punch, the value of 0.7268 for a cone indenter and the value of 0.75 for a spherical or paraboloidal indenter. The quantities h_{max} and hi are determined from the experimental data.

The area function $A(hc)$ depends on the shape of the indenter. For a Berkovich indenter (a three-sided pyramid with angles between the axis of symmetry and a face of 35.3º) it takes the form

$$A\left(h_c\right) = 24.5h_c^2 \tag{16}$$

The hardness H_c is defined by

$$H_c = \frac{P_{max}}{A_c} \tag{17}$$

where P_{max} is the peak indentation load and Ac is the contact area under maximum load. This definition of hardness is different from that used in an imaging indentation test. In the latter case the area is the residual area measured after the indenter is removed, while in the nanoindentation test the area is the contact area undermaximum load. This distinction is important for materials with large elastic recovery, for example rubber. A conventional hardness test with zero residual area would give infinite hardness, while a nanoindentation test would give a finite hardness.

Equation (16) gives the area function $A_{(hc)}$ for an ideal Berkovich indenter. However, real tips are never ideally sharp and generally, are characterized by a radius of curvature at the tip. In such cases the function $A_{(hc)}$ must be determined. Methods for determining $A_{(hc)}$ include the TEM (transmission electron microscope) replica method in which replicas of indentation are made and their areas are measured in TEM, the SFM (scanning force microscope) method in which the indenter tip is measured with a sharper SFM tip of known shape and a method based on Equation (11) applied to a number of materials with known Young's modulus.

The above analysis suggests the following procedure for the determination of Young's modulus and hardness in nanoindentation from Equations (11) and (17):

i. Use Equation (11) to fit the unloading data.
ii. Find *hc* from Equation (14) using the value of depth at maximum load, h_{max}, the slope of the fit at *P*max to obtain *hi* and the appropriate value of ε.
iii. Use the area function $A_{(hc)}$ of the indenter to find the contact area at maximum load from the contact depth h_c.

From the value of *Er* determined from Equation (12) the elastic modulus, *E*, of the material is determined from Equation (10) when the elastic modulus *Ei* of the indenter is known.

The accuracy of such a measurement depends on the film and substrate properties and on the indentation depth as a fraction of the total film thickness. In general, the error due

to the substrate effect increases with increasing indentation depth and with increasing elastic mismatch between film and substrate. To minimize the effect of the substrate on the measurement, the indentation depth is often limited to less than 10% of the film thickness. This empirical rule is not always reliable, especially if the elastic mismatch between film and substrate is large. The 10% rule is also not useful for very thin films when experimental issues make it difficult to obtain accurate results for very shallow indentations. Evidently there exists a need for a method that can be used to analyze thin-film indentation data for indentation depths where the substrate effect cannot be ignored.

METHODS OF SPECTROSCOPY

Fourier transform infra-red (FTIR) spectroscopy

The total internal energy of a molecule in a first approximation can be resolved into the sum of rotational, vibrational and electronic energy levels. Infrared spectroscopy is the study of interactions between matter and electromagnetic fields in the IR region. In this spectral region, the EM waves mainly couple with the molecular vibrations. In other words, a molecule can be excited to a higher vibrational state by absorbing IR radiation. The probability of a particular IR frequency being absorbed depends on the actual interaction between this frequency and the molecule. In general, a frequency will be strongly absorbed if its photon energy coincides with the vibrational energy levels of the molecule. IR spectroscopy is therefore a very powerful technique which provides fingerprint information on the chemical composition of the sample. FTIR spectrometer is found in most analytical laboratories.

An infrared spectrum represents a fingerprint of a sample with absorption peaks whichcorrespond to the frequencies of vibrations between the bonds of the atoms making up the material. Because each different material is a unique combination of atoms, no two compounds produce the exact same infrared spectrum. Therefore, infrared spectroscopy can result in a positive **identification** (qualitative analysis) of every different kind of material. In addition, the size of the peaks in the spectrum is a

direct indication of the **amount** of material present. With modern software algorithms, infrared is an excellent tool for quantitative analysis.

A method for measuring all of the infrared frequencies **simultaneously**, rather than individually, was needed. A solution was developed which employed a very simple optical device called an i**nterferometer**. The interferometer produces a unique type of signal which has all of the infrared frequencies "encoded" into it. The signal can be measured very quickly, usually on the order of **one second** or so. Thus, the time element per sample is reduced to a matter of a few seconds rather than several minutes. The resulting signal

is called an **interferogram** which has the unique property that every data point (a function of the moving mirror position) which makes up the signal has information about every infrared frequency which comes from the source. This means that as the interferogram is measured, all frequencies are being measured **simultaneously**. Thus, the use of the interferometer results in extremely fast measurements. Because the analyst requires a **frequency spectrum** (a plot of the intensity at each individual frequency) in order to make an identification, the measured interferogram signal can not be interpreted directly. A means of "decoding" the individual frequencies is required. This can be accomplished via a well-known mathematical technique called the **Fourier transformation**. This transformation is erformed by the computer which then presents the user with the desired spectral information for analysis. However the FTIR spectrometer operates on a different principle called *Fourier transform*. The mathematical expression of Fourier transform can be expressed as

$$F(\omega) = \int_{-\infty}^{+\infty} f(x) e^{i\omega x} dx \qquad (18)$$

And the reverse Fourier transform is

$$f(x) = \frac{1}{2\pi} \int_{-\infty}^{+\infty} F(\omega) e^{-i\omega x} d\omega \tag{19}$$

where ω is angular frequency and x is the optical path difference in our case. $F(\omega)$ is the spectrum and $f(x)$ is called the interferogram.

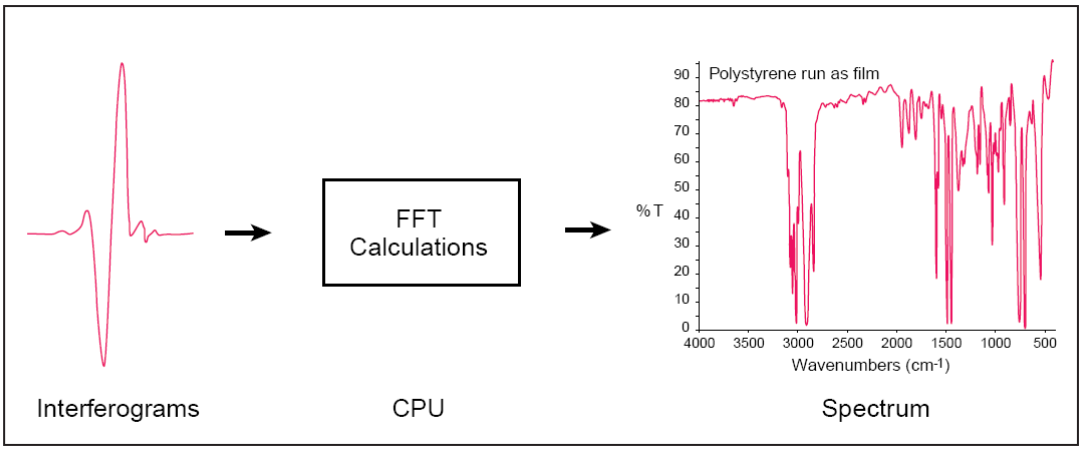

Figure 19 Definition of interferogram and spectar

Raman spectroscopy

When light is scattered from a molecule or crystal, most photons are elastically scattered. The scattered photons have the same energy (frequency) and, therefore, wavelength, as the incident photons. However, a small fraction of light (approximately 1 in 107 photons) is scattered at optical frequencies different from, and usually lower than, the frequency of the incident photons. The process leading to this inelastic scatter is termed the Raman effect. Raman scattering can occur with a change in vibrational, rotational or electronic energy of a molecule. If the scattering is elastic, the process is called Rayleigh scattering. If it's not elastic, the process is called Raman scattering.

The Raman effect arises when a photon is incident on a molecule and interacts with the electric dipole of the molecule. In quantum mechanics the scattering is described as an excitation to a virtual state lower in energy than a real electronic transition with nearly coincident de-excitation and a change in vibrational energy. The scattering event occurs in 10^{-14} seconds or less. The virtual state description of the scattering is shown in Figure 20.

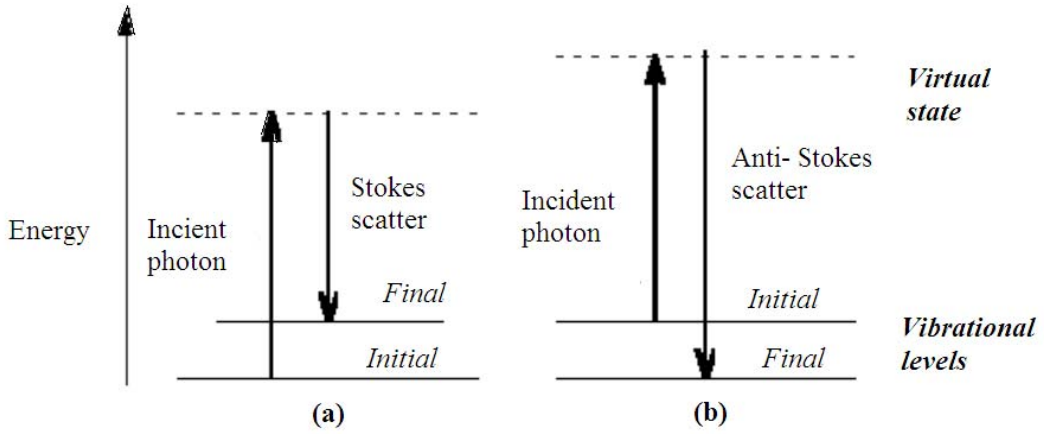

Figure 20 Energy level diagram for Raman scattering; (a) Stokes scattering, (b) anti-Stokes scattering

A complex molecule can absorb and emit energy by interacting with photons that can excite molecules to higher vibrational states. These vibrations are quantized and are called the normal modes of vibration of the molecule. A linear molecule with N atoms has 3N-5 normal modes, while a non-linear molecule has 3N-6 normal modes. The motion that characterizes each normal mode can be:

• Bending motion between three atoms connected by two bonds

• Stretching motion between two bonded atoms

• Out-of-plane deformation modes that change an otherwise planar structure into a nonplanar one

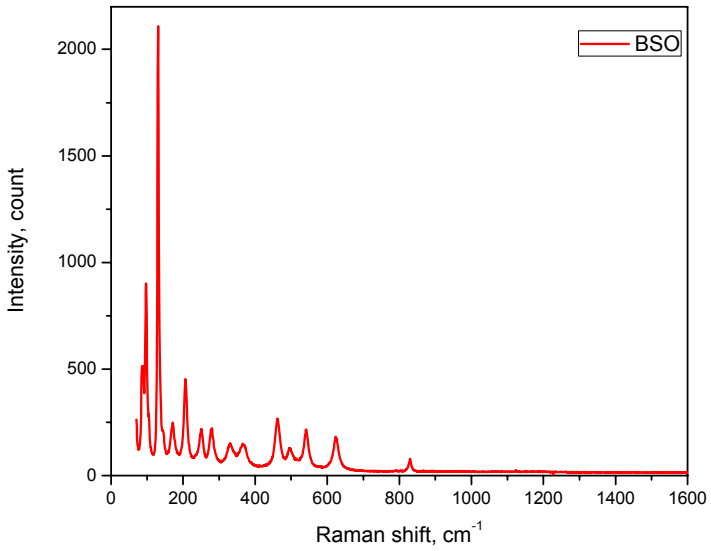

Figure 21 Raman shifto of BSO single crystal

THERMAL PROPERTIES

Differential Scanning Calorimetry (DSC)

Differential scanning calorimetry (DSC) is an experimental technique to measure the heat energy uptake that takes place in a sample during controlled increase (or decrease) in temperature. The DSC can be used to obtain the thermal critical points like melting point, enthalpy specific heat or glass transition temperature of substances. The schematic principle of the DSC is described in Figure 24.

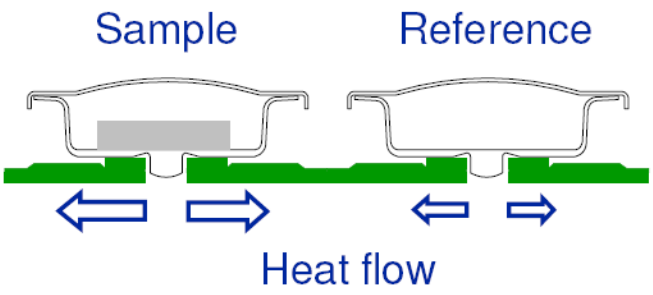

Figure 22 Principle of DSC

The sample and an empty reference crucible is heated at constant heat flow. A difference of the temperature of both crucibles is caused by the thermal critical points of the sample and can be detected.

At the simplest level it may be used to determine thermal transition ("melting") temperatures for samples in solution, solid, or mixed phases (e.g. suspensions). But with more sensitive apparatus and more careful experimentation it may be used to determine absolute thermodynamic data for thermally-induced transitions of various kinds. Formerly this was more the realm of the dedicated specialist, but now with

the ready availability of sensitive, stable, user-friendly DSC instruments, microcalorimetry has become part of the standard repertoire of methods available to the biophysical chemist for the study of macromolecular conformation and interactions in solution at reasonable concentrations. And, to the extent that thermal transitions might be affected by ligand binding, DSC can provide useful information about protein-ligand binding. The advantages of calorimetric techniques arise because they are based on direct measurements of intrinsic thermal properties of the samples, and are usually noninvasive and require no chemical modifications or extrinsic probes. Furthermore, with careful analysis and interpretation, calorimetric experiments can directly provide fundamental thermodynamic information about the processes involved.

OPTICAL PROPERTIES

Spectroscopic Ellipsometry

Ellipsometry is a nonperturbing optical technique that uses the change in the state of polarization of light upon reflection for the in-situ and real-time characterization of surfaces, interfaces, and thin films.

In ellipsometry, a collimated beam of monochromatic or quasi-monochromatic light, which is polarized in a known state, is incident on a sample surface under examination, and the state of polarization of the reflected light is analyzed. From the incident and reflected states of polarization, ratios of complex reflection coefficients of the surface for the incident orthogonal linear polarizations parallel and perpendicular to the plane of

incidence are determined. These ratios are subsequently related to the structural and optical properties of the ambient-sample interface region by invoking an appropriate model and the electromagnetic theory of reflection. In a typical scheme, Fig. 23, the incident light is linearly polarized at a known but arbitrary azimuth and the reflected light is elliptically polarized. Measurement of the ellipse of polarization of the reflected light accounts for the name ellipsometry Incident linearly polarized light of arbitrary azimuth θ is reflected from the surface S as elliptically polarized. *p* and *s* identify the linear polarization directions parallel and perpendicular to the plane of incidence and form a right-handed system with the direction of propagation. ϕ is the angle of incidence.

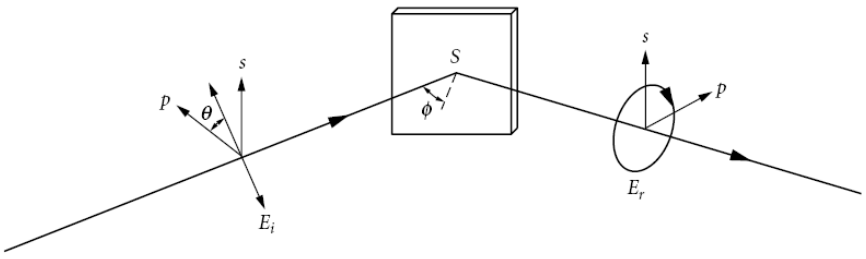

Figure 23 Scheme of ellipsometri mesuremen

A complex index of refraction can be presented with the following equation:

$$\tilde{n} = n + i\kappa \tag{20}$$

where, the real part *n* is the refractive index indicating the phase speed, while κ is *extinction coefficient*, which indicates the amount of absorption loss when the light propagates through the material. Both *n* and κ are dependent on the wavelength.

Time resolved laser induced fluorescence measurements

A number of studies have appeared on the detection, spectroscopy and lifetime measurements of organic molecules based on time resolved laser-induced fluorescence (TR-LIF) techniques [89- 91]. This technique is one of the most ensitive approaches in research for a variety of analytical applications in the fields of life sciences, biophysics and biomedical applications. The laser induced breakdown spectroscopy (LIBS) is a sensitive tool for a rapid identification the elemental composition of a sample regardless the aggregate states and with a little sample preparation. The LIBS technique could be useful for detection of toxic elements in food. TR-LIF and LIBS have similar hardware requirements. In this paper, we analyze some of characteristics of TR-LIF/LIBS system implemented in our laboratory, considering the fact that the excitation part of the system is based on nanosecond Nd:YAG laser and Optical Parametric Oscillator (OPO). The fluorescence detection part of our system is based on picosecond streak camera.

The laser is more than powerful enough (365 mJ at 1064 nm, variable OPO output >5 mJ) for LIBS, but somehow slow (the length of fundamental laser harmonic output pulse is about 5 ns) for fluorescence measurements in our present area of interest, namely plants and food products. Fortunately, the pulse length of tunableOPO output (320–475 nm) is less than 1 ns, so by means of a correct deconvolution procedure it is possible to measure the fluorescence lifetimes in the range as small as a few nanoseconds.

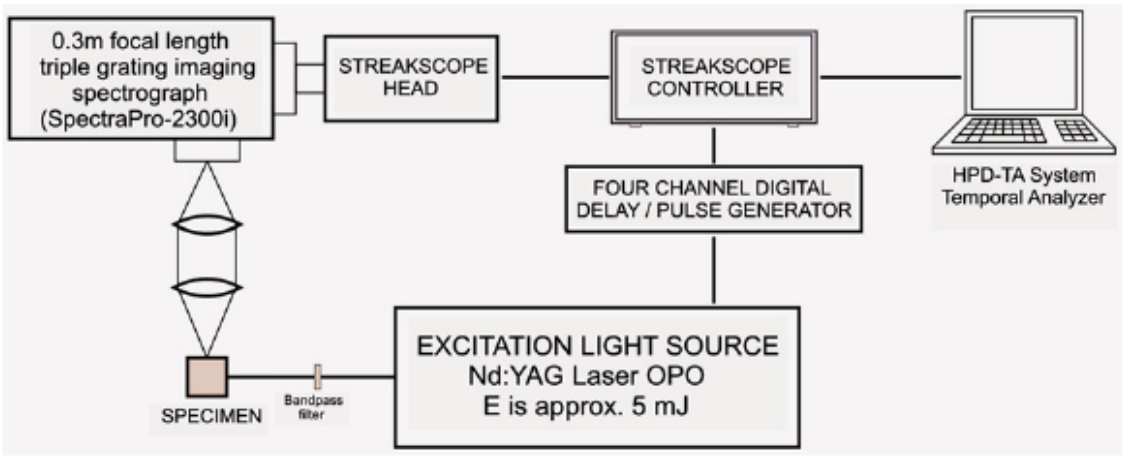

Figure 24 Schematic illustration of experimental setup for TR-LIF spectroscopy [91]

The laser induced fluorescence in the samples is recorded using streak camera. The testing of system was obtained by using the fluorescent dyes Rhodamine B and Fluorescein ethanol solutions. Comparing obtained results with the published data we verified the temporal analyzing capabilities of our TR-LIF system. The experimental set-up used in this study consists of excitation and detection part (Fig. 24). Pulsed excitation was provided by a tunable Nd-YAG laser system (Vibrant model 266 made by Opotek, Inc.). The declared output level at 266 nm is up to >50 mJ, with pulse duration of about 5 ns and repetition rate of 10 Hz. This system incorporates the Optical Parametric Oscillator (OPO) that is pumped by the fourth harmonics of the laser at 266 nm. After passing through the OPO pulse length is reduced to less than 1 ns and energy output is ~5 mJ. The output of the OPO can be continuously The laser induced fluorescence in the samples was collected at 90º from the excitation and dispersed by a 0.3 m focal length triple grating imaging spectrograph (SpectraPro-2300i). For measurements presented in this paper the grating of 50 lines/mm was used covering a 330 nm spectral range with the resolution of about 3.6 nm. The blaze wavelength of the grating is 600 nm, so the variation of grating spectral response in the recorded range is minimal.

To modify the TR-LIF system for LIBS, the band pass filter should be substituted by a focusing lens. Even OPO output has enough energy to induce plasma forming on the focused spot. The laser induced fluorescence in the samples is recorded using streak scope (Hamamatsu model C4334-01) with integrated video streak camera. The fundamental advantage of the streak scope is its two dimensional nature, that is especially important in measuring time-resolved fluorescence spectra. The data have been acquired using High Performance Digital Temporal Analyzer (HPD-TA) software.

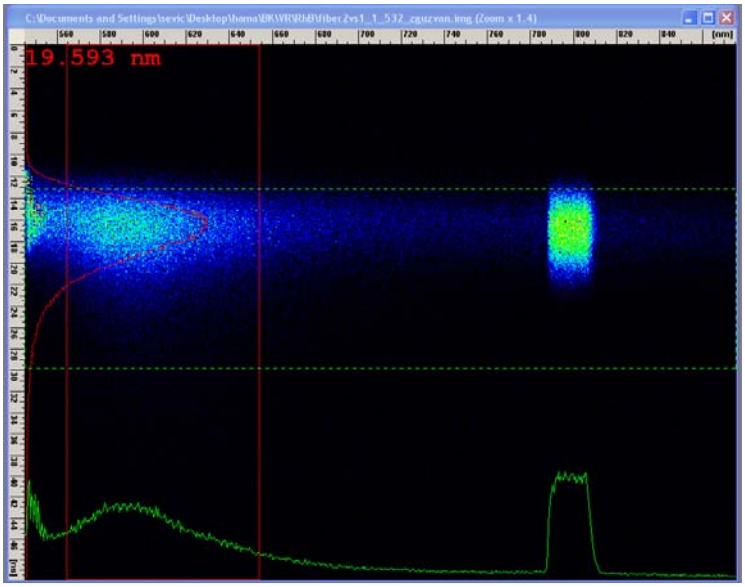

Figure 25 Streak image of the fluorescence spectra

The results can be presented in form of absorbance and emission spectra (Figure 20, 21). The absorbance band and emission band are specific of material according electron structure.

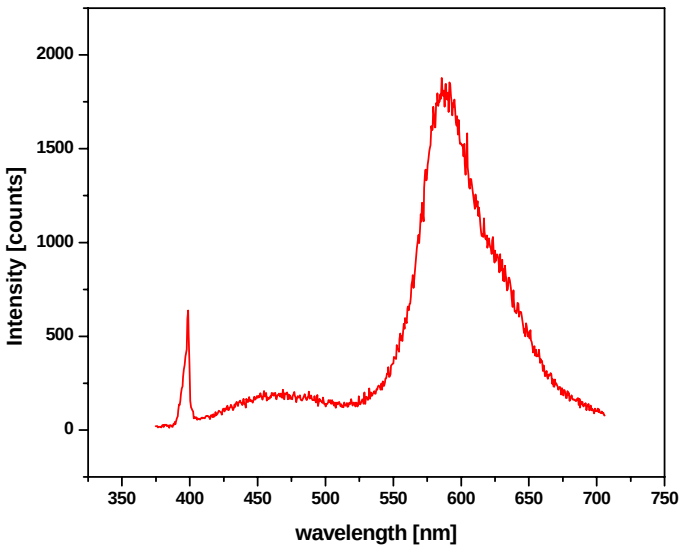

Figure 26 Absorbance and emission spectra of fluorescence

FUTURE PERSPECTIVE OF POLYMER SCINTILLATION COMPOSITES

Scintillating composites can find many potential applications due to their low cost and ease of preparation, high density and efficiency, size and compactness compared to other scintillation counters.

These composites could be used for a variety of applications which include gamma-ray spectroscopy, contamination surveys, land surveys and aerial radiological surveys for the presence of gamma- emitting radio nucleides. They can be used as detectors for safety detector requirements like in a scanner to rapidly identify a suspect luggage in a few cubic meter large container moving across the inspection device and remote detection of fissile materials These detectors can be used for laboratory applications, such as nuclear material processing, laboratory research activity, to field applications such as nuclear waste processing and management, nuclear explosion monitoring, maritime security and radioactive material transportation monitoring.

Scintillating composite fibers could find applications in medical imaging techniques, where a radioisotope is injected into the body, which produces ionizing radiation that can be detected by inserting a scintillating fiber sensor into the diseased part. Scintillating fibers can also be used in the form of an array for imaging purposes in order to determine something about the physiology or anatomy of the target organ.

Using scintillation optical fiber array coupled with a CCD can be considered to construct another kind X-ray digital imager [92]. In such a detector, a portion of light (converted from incoming X-ray within a fiber) is channeled along the fiber through total internal reflection, and the Extra Mural Absorber (EMA) would absorb the remainder. The scattered radiation in a fiber causes a uniform background. Such a design, in principle, does not require the length compromise of the fiber and the spatial resolution. PSFs are commercially available with various dimensions,and are less expensive comparing to bulk scintillation materials. Thus the design can reduce the cost and the complexity significantly. More importantly, PSFs are flexible and can be easily built into an area detector with geometry best matched with that of the object being imaged to achieve maximum efficiency.

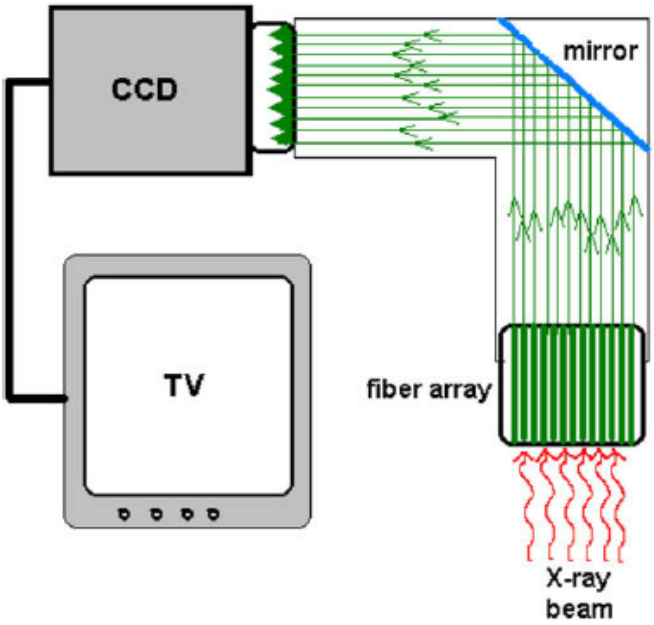

a)

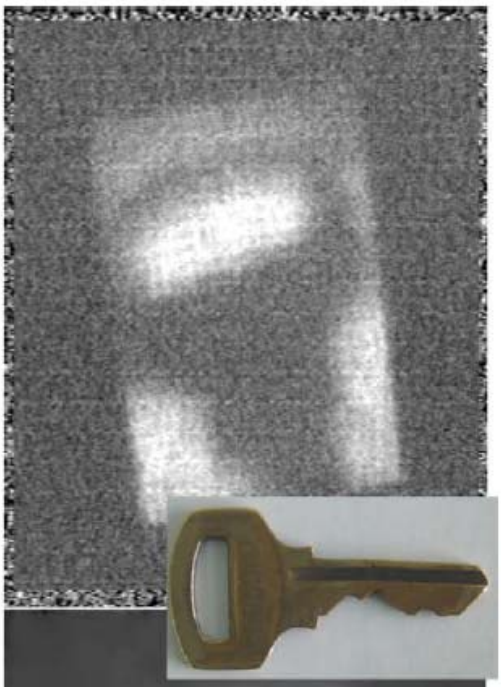

b)

Figure 27a) Schematic of the experiment setup (coupling of the PSF array CCD); b) Radiogram that was taken by PSF array **[92]**

Among other nanostructures, polymer nanofibers are novel, cheap, and flexible building blocks potentially employable in functional, optical, and electronic nanoscale circuits. Moreover, the addition of active components (i.e., nanoparticles or molecular species) to the ES polymer solution allows one to obtain composite nanofibers with specific functionalities. In particular, recently achieved light-emitting electrospun nanofibers are currently under study for their waveguiding properties, and for their photo [83] and electroluminescence. These nanofibers can be assembled in ordered structures and arrays and they can potentially be used to realize fully plastic, nano-microscale optical devices and circuits. Achieving miniaturized light-emitting sources is also gathering interest for integration in sensors and labon chips. The remarkable potential of electrospun, flexible gain nanofibers as active waveguides and lasers are presented. As a prototype system, demonstrate single mode optically pumped lasing sources based on individual electrospun nanofibers emitting at 585nm with linewidth of 0.3nm and excitation threshold fluence as low as 60mJ cm^{-2} [93]. The electrospun nanofibers was processed from solution PMMA in chloroform and with addition of Rhodamine 6G.

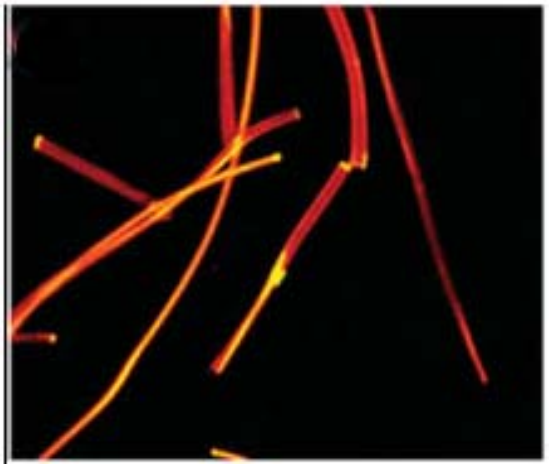

Figure 28 Fluorescence images of fibers with Rh 6G

EXPERIMENTAL PART

SYNTHESIS CHARACTERIZATION AND MECHANICAL PROPERTIES OF $BI_{12}SiO_{20}$ - PMMA COMPOSITE FILMS

Materials

Single crystals of $Bi_{12}SiO_{20}$ were grown by the Czochralski technique using a MSR 2 crystal puller controlled by a Eurotherm [94]. The single crystal was grown in an air atmosphere from synthesized Bi_2O_3 and SiO_2. The obtained single crystal grew in the <111> direction and no core were observed. Powdering of synthesized single crystal was conducted by hand grinding. The particle size was determinated by image analysis of SEM photos with the average size of 3.67μm. The polymer component of the composite was commercially available heat resistant injection grade PMMA pellets, Acryrex® CM-205 (M_w= 90400, Chi Mei Corporation, Taiwan), with no detected solute according RoHS Directive. Acetone was purchased at Zorka Pharma, Serbia.

Preparation of specimens

Thin films of pure PMMA and composites with 0.5 wt% and 1.0 wt% of BSO were prepared with a dispersion casting method. Samples were obtained by dissolving PMMA in acetone for 24 hours and then adding BSO powder to the solution with continuous stirring. The mixture was then poured in the Petri dish and left inside an oven at constant temperature of 45 °C for another 24 h. Produced thin films had average thickness of 0.76 mm.

Characterization of samples

The X-ray diffraction (XRD) data for $Bi_{12}SiO_{20}$ single crystals was measured using a Cu Kα radiation and a monochromator (Model Philips PW 1710 diffractometer) under the following experimental conditions: 40 kV and 20 mA, 20 °< 2ϑ < 80°, with a step of 0.02° for 0.5 s. Infrared (IR) spectrum of the powder, pure PMMA and the composites were obtained with a Fourier transform infrared (FTIR) transmission-KBr disk spectroscopy, Hartmann & Braun, MB-series. The scanning range of FTIR was between 4000 and 400 cm^{-1} with a resolution of 4 cm^{-1}. The differential scanning calorimetry (DSC) measurements were conducted using a TA Instrument, TA DSC Q10 calibrated with indium standards. The temperature range was from 30 °C to 130 °C at a heating rate of 10 °C/min with a dynamic nitrogen flow of 50 mL/min. The samples were heated up to 130 °C, kept at 130 °C for 5 min to erase thermal history, and cooled down to 30 °C at the same cooling rate. A second heating was done on the each sample. The glass transition was determined using the midpoint of the initial transition slopes.

SEM imaging of BSO powder was performed on a scanning electron microscope (SEM), Jeol JSM 5800, operated at 20 keV, in order to establish the size of the particles. Dispersion and deagglomeration of particles in the composite films were investigated using FESEM (TESCAN MIRA 3). Size distribution of particles was obtained through analysis of SEM images using program *Image Pro Plus 6.0*. Spectroscopic ellipsometry method for measuring refractive indices of pure PMMA and composites was performed with SOPRA GES5E IRSE spectroscopic ellipsometer in a wavelength range from 400 to 800 nm. The Raman spectra were obtained by the micro-Raman analyzed using Jobin Yvon T64000 spectrometer, equipped with nitrogen cooled charge-coupled device detector. The measurements were performed at 20 mW during 200 s at room temperature. Spectral range of Raman was from 50 to 900 cm^{-1}, in back scattering geometry. The tensile testing of samples was performed on Universal hydraulic tensile-compressive testing machine INSTRON, Germany. Hysitron TI 950 Triboindenter with a Berkovich diamond tip and in-situ imaging scan mode was used for nanoindentation tests. The hardness and reduced elastic modulus were calculated from the curves using the Oliver and Pharr method [88]. The

indentation maximum load was set to be 2 mN for all samples. The loading and unloading times as well as the hold time at the peak force were set to 25 s each.

Results and Discussion

XRD analysis

XRD analysis was performed to authenticate the single crystall BSO. Figure 29 presents the XRD pattern of $6Bi_2O_3 + SiO_2$. The diffractometer was used in the 2θ range from 15º to 80º. XRD indicates that all peaks belong to the $Bi_{12}SiO_{20}$ phase, which is in good agreement with the JCPDF Card No. 37-0485. The unit cell of $Bi_{12}SiO_{20}$ was calculated by the least square method using all 21 reflections including more $K\alpha_2$ for 5 reflections. Many of the reflections correspond to $Bi_{12}SiO_{20}$ crystals with the parameter of cubic I-centered cell a = 1.01067 nm, and x = 12. The calculated lattice parameter is a = 1.0096 nm, which is in good agreement with published data [71].

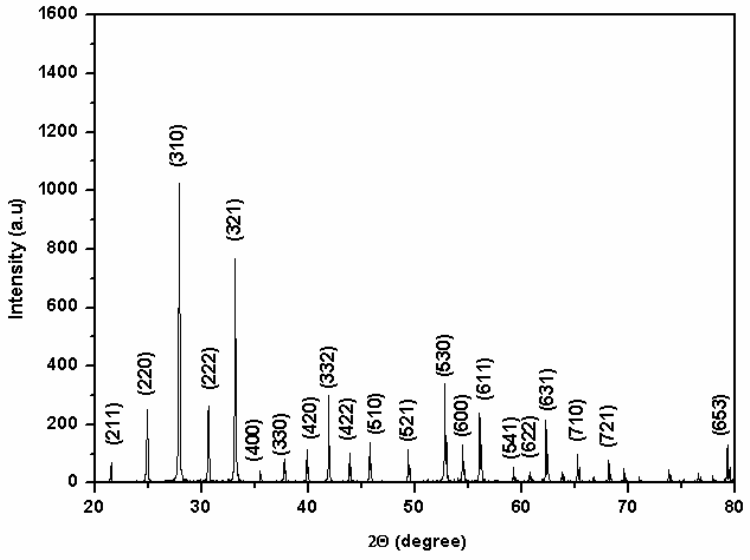

Figure 29 X-ray diffraction results of BSO single crystal

FTIR spectrum

The FTIR spectra of $Bi_{12}SiO_{20}$ powder, PMMA and composites are presented in Fig. 30. The FTIR spectrum of BSO shows well-defined peaks located at 832, 606, 577, 528 and 468 cm^{-1}. The peak located at 832 cm^{-1} is due to the stretching vibration mode of Bi–O–Si bonds. The shift observed in the bands location can be associated with the difference between the atomic masses of silicon and bismuth atoms. The peak at 606 cm^{-1} is related with cationic vibrations in the network of Bi-O vibration. The peak located at 577 cm^{-1} is associated with the bending vibration mode of distorted tetrahedron formed by $(SiO_4)^{4-}$groups. The band located at 528 cm^{-1} is assigned to deformation vibration of isolated $(SiO_4)^{4-}$ groups. The band located at 468 cm^{-1} is related with Si-O bond rocking and interaction by $[BiO_6]$ polyhedron. The peaks at 2926 cm^{-1} and 1733 cm^{-1} are assigned to C–H stretching and C=O stretching vibrations, respectively in PMMA. The absorption peaks of PMMA (1439, 840, 750 and 440 cm^{-1}), and the vibration bands of PMMA (3458, 1385, 1146 and 990 cm^{-1}), are observed in the spectrograms. In the FTIR spectrum of composites there are well defined peaks for PMMA and some of the vibration modes of Bi–O–Si bonds (832, 528 and 468) cm^{-1} [26]. This means that BSO crystals in the composite have been identified and that no other bounds with PMMA were created during the processing.

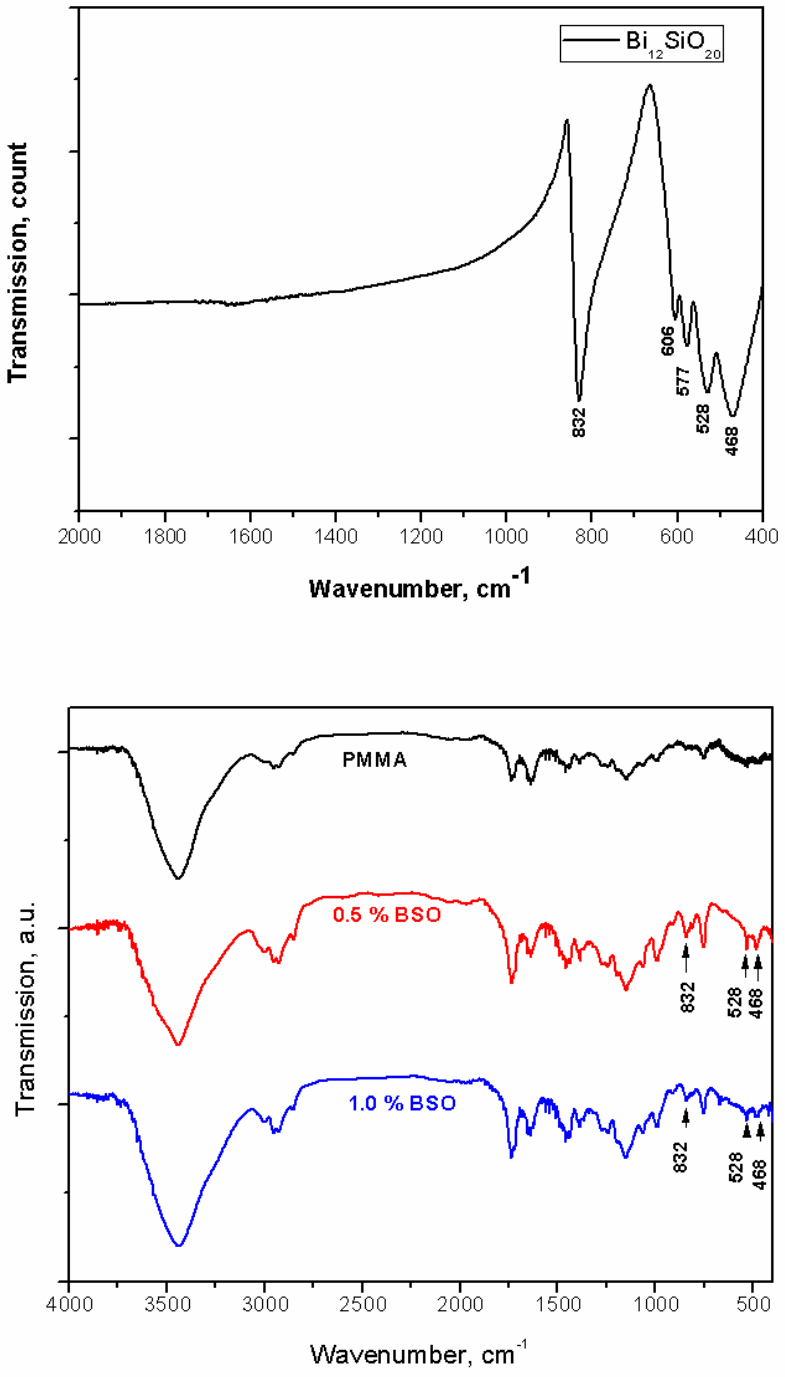

Figure 30 FTIR spectrum of a) BSO powder and b) pure PMMA and BSO-PMMA composites

Raman spectroscopy

The Raman spectra of $Bi_{12}SiO_{20}$ single crystals and the composite in spectral range from 50 to 1000 cm^{-1} at room temperature is shown in Fig. 31. The spectrum of $Bi_{12}SiO_{20}$ exhibits intense modes at about 130, 155, 190, 260, 315, 445, 480, 530, 610, 770, 815 and 830cm^{-1}. The intensity modes at about 155, 260, 315 and 530 cm^{-1} are associated with the 'breathing' of Bi, O1 and O2 atoms. The modes at about 130, 260, 445 and 610 cm^{-1} show Bi and O1, O2, O3 vibrations elongating the cluster along either <100> or <001>, <100> or <010>, respectively. The mode at 480 cm^{-1} can be assigned to Bi-O1 stretching and deformation of MO_4 tetrahedral (symmetry type *TO+LO*). The mode at 770 cm^{-1}, and modes at 815 and 830 cm^{-1} are characteristic of symmetric stretching of MO_4 tetrahedral and anti-symmetric stretching of MO_4 tetrahedral, respectively. Raman spectroscopy of composites has given same modes as for pure BSO.

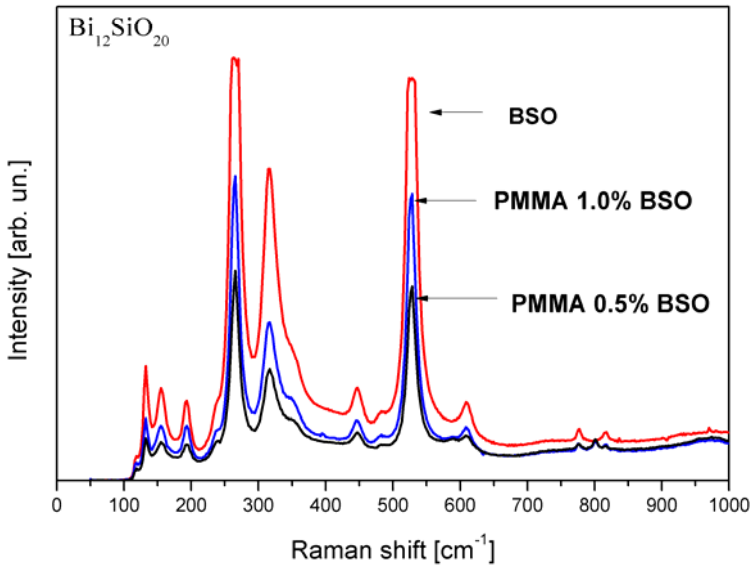

Figure 31 Raman spectra of BSO crystal and PMMA-BSO composites

SEM analysis

SEM micrograph of $Bi_{12}SiO_{20}$ powder, presented in Figure 32, clearly shows that the formation of aggregates has occurred. Aggregates are considered also by one of program features. The program evaluates possible clusterization of the particles and offers the possibility to calculate the number of particles in the cluster. Only the unique particles were considered for the evaluation of particle diameter. Other possibility given by image analysis would be to split large clusters into individual objects using the software but this was not necessary as enough individual particles were visible in the images given for measurements. Every particle represents an object in the analysis. For each object the mean diameter is measured as average length of diameters measured at 2 degree intervals and passing trough object's centroid. Statistical analysis of images is presented on Table 1.

Table 1. The statistical data of measurements of BSO particles

Stats	Area	Diameter (mea	Roundness	Cluster	Fractal Dimen
Min	1.301763	1.101993	1.125423	1	1.073405
(Obj.#)	401	190	338	30	265
Max	300.1865	18.93526	19.58049	104	1.3462
(Obj.#)	282	282	402	282	274
Range	298.8848	17.83326	18.45507	103	0.272795
Mean	17.49672	3.762748	3.772043	5.782609	1.17712
Std.Dev	34.80001	2.793826	3.163077	12.00419	0.071061
Sum	2012.123	432.7161	433.7849	665	135.3688
Samples	115	115	115	115	115

The average particle size is 3. 67 μm. FESEM image of composite films also shows aggregates of BSO particles (Figure 33).

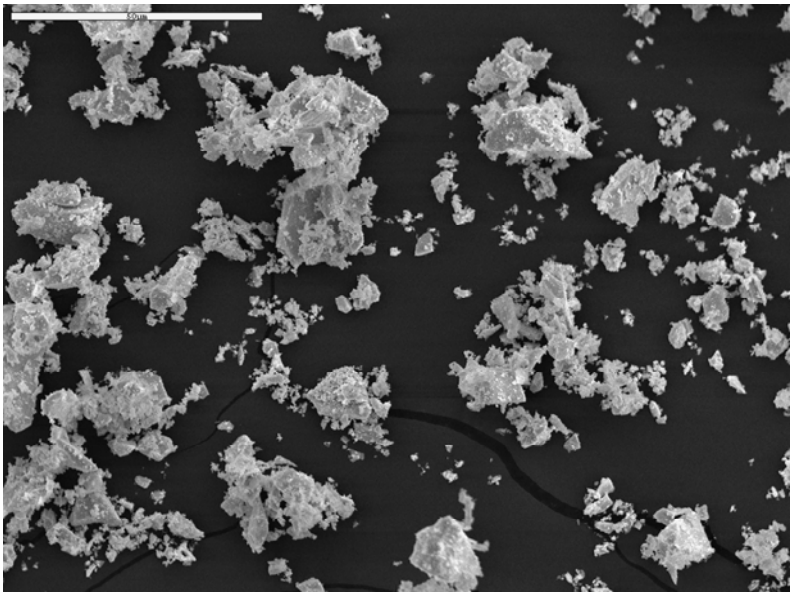

Figure 32 SEM micrograph of BSO crystal particles

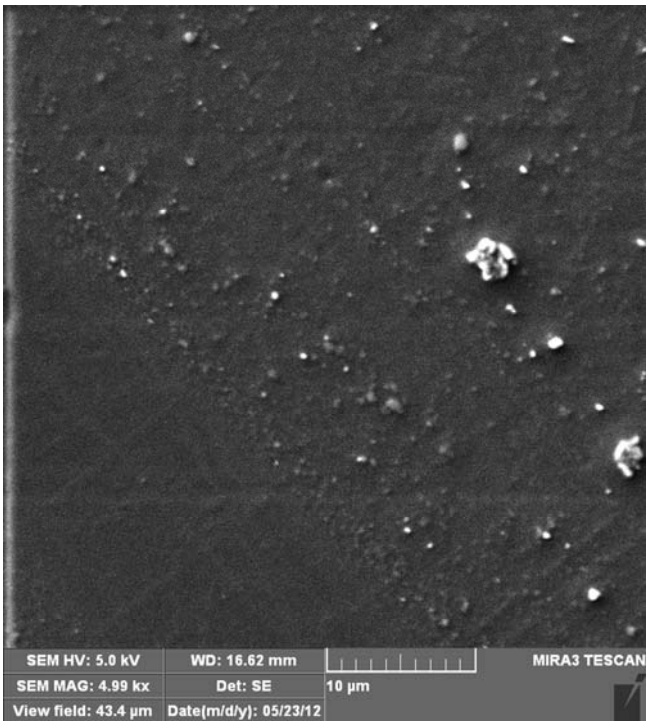

Figure 33 FESEM image of BSO-PMMA composite

DSC analysis

DSC analysis investigated the influence of BSO powder to thermal stability of composite. DSC of pure PMMA and composites is presented in Figure 34. The results show that the glass transition of pure PMMA is shifted towards the lower temperatures, as compared with the bulk polymer obtained by molding of PMMA pellets, without any solvent (*Tg* = 101.18 °C) [34]. The effect of the solvent contained in the film decreases the glass transition temperature (T_g) of the polymer and composites [95]. As the BSO content increased, *T*g of the composites slightly increased, so the thermal stability was improved. The T_g of composite with 0.5 % wt BSO was raised by 8.0 % while the *Tg* of composite with 1.0% wt BSO was increased by 9.1 %. This result could suggest that a chemical bond was not formed between polymer and particles, but the particles behaved as highly functional physical crosslink and increased the *Tg*.

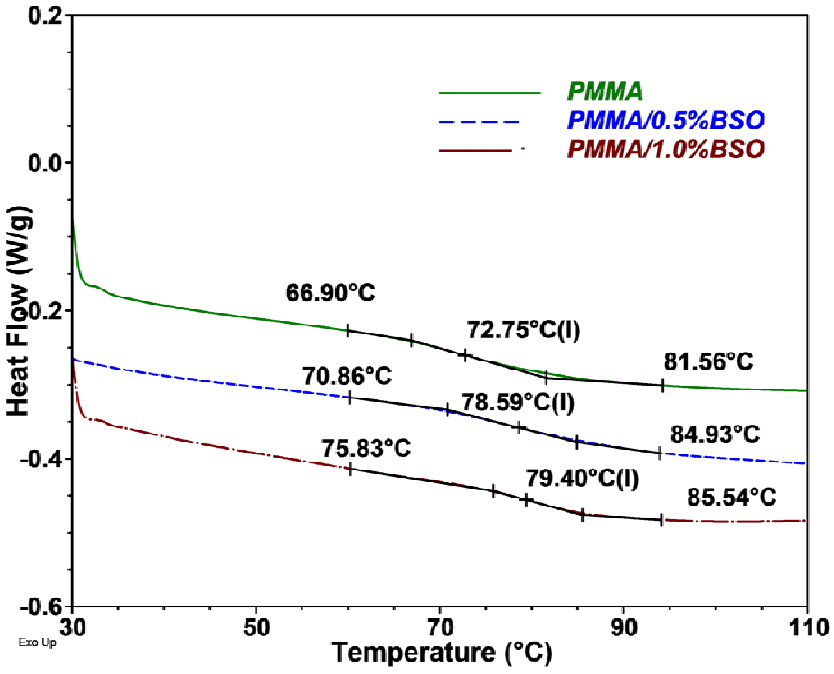

Figure 34 DSC of pure PMMA and composites

Refractive index

Figure 35 presents refractive index of pure PMMA and the composites in visible region of spectra. Light entering the particle-polymer interface will experience reflection, refraction, diffraction and interference. When the incident ray of light reaches the BSO-polymer interface, due to the higher refractive index, the ray refracts towards the crystal phase. It means that with the addition of BSO particles it is possible to make an optically denser medium in which rays of light can stay longer. Accordingly, the refractive index of the composite itself increases with the content of particles according to the Maxwell-Garnett effective medium expression [96, 97]. However, the cumulative effect is present because the particle dimension also influences the refractive index as shown in the literature. [96, 98]. So, this makes it possible for the composite BSO-PMMA to be used as a Light Trapping Medium. As expected, due to a higher refractive index of the BSO powders, the addition of particles yields an increase of the polymer composites refractive index in relation to pure PMMA. Also, the refractive index of composites increased as the BSO content increased, after wavelength of 400 nm.

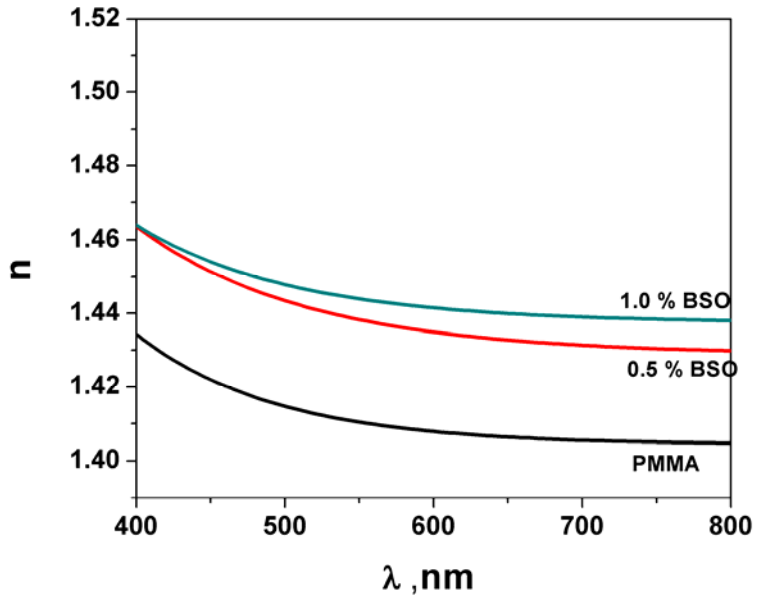

Figure 35 Refractive indices of pure PMMA and BSO-PMMA composites

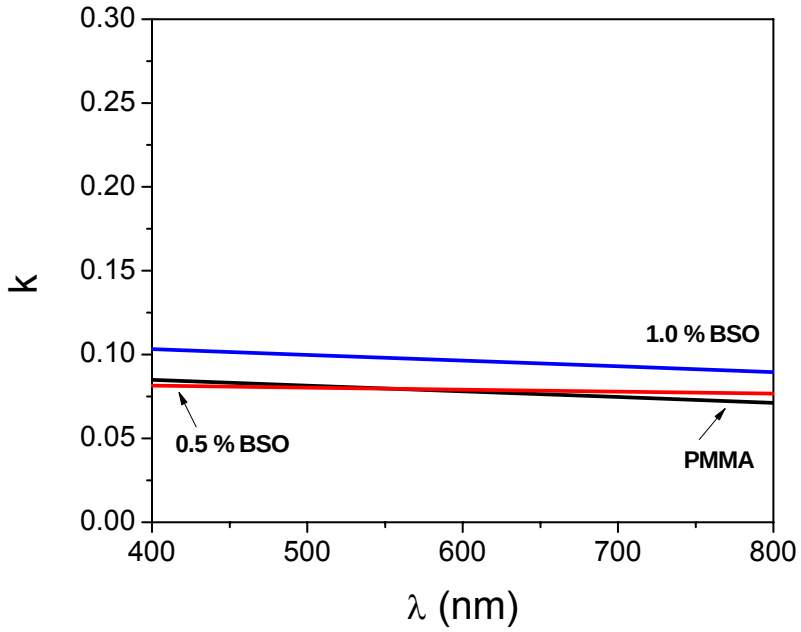

Figure 36 ***Extinction coefficient of pure PMMA and BSO-PMMA composites***

Extinction coefficient of pure PMMA and composites in visible region of spectra are presented in Figure 36. It is obvious that the index of refraction of composites increases as the BSO content increased. The coefficient of extinction shows good transparence of composite in visible range of spectra.

Tensile test

Results of a tensile test are presented in Table 2. A study of mechanical properties showed that a higher content of the fillers in the polymer-matrix composites results in an increase of the modulus of elasticity, the tensile stress, and tensile strength. It is obvious that even in the absence of specific interactions with the polymer the particles reduced the overall mobility of the polymer chains [99]. This results is in accordance with the results of a tensile test and DMA of composite bars in which the tensile strength and modulus of elasticity increased in composites with higher particle content [12].

Table 2 Tensile test results

C_{BSO}, wt%	R_m, MPa	*e*, %	*E*, GPa
0.0	24.60	2.03	1.153
0.5	37.65	3.51	1.206
1.0	25.84	2.19	2.600

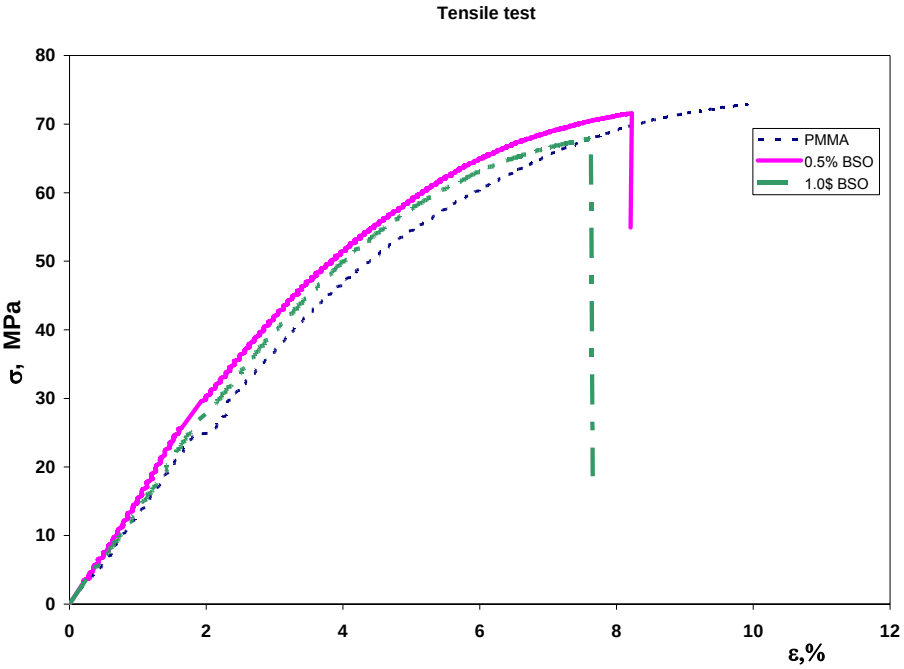

Figure 37 ***Stress-strain curves for pure PMMA and BSO-PMMA composites***

Nanoindentation

Nanoindentation test results are listed in Table 3 and the experimental curve shows dependence of depth in loading-unloading cycle. Figure 38 (a) shows typical force–depth curves obtained in the nanoindentation tests for neat PMMA film and composites with BSO. The curves appear to be with continuity and without pop-in or pop-out in both loading and unloading phases. Figure 38 (b) displays the plastic imprint of the

indent for the sample with 1.0 wt% BSO with the scan trace in the vicinity of the indent. In-situ imaging mode used for scanning the surface reveals the absence of cracks and fractures around the indent.

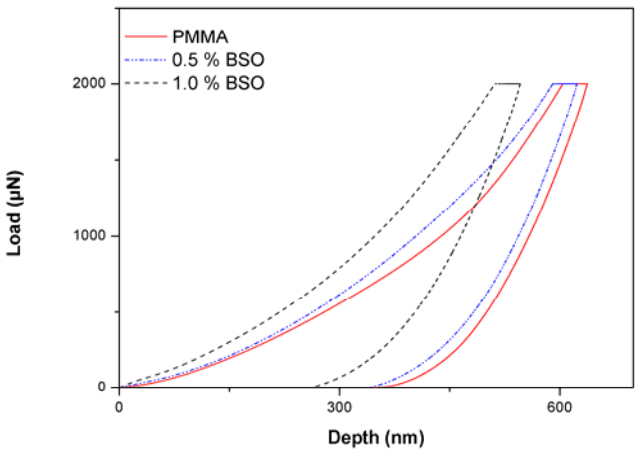

a)

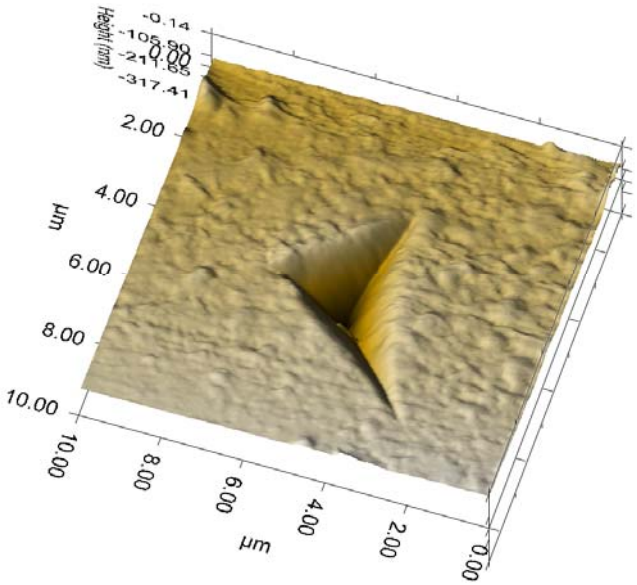

b)

Figure 38 a) Force-depth curves for pure PMMA and composite films; b) Indent plastic imprint of the PMMA-0.5 wt% BSO sample

The results of reduced elastic modulus and hardness for neat polymer and composites with 0.5 and 1.0 wt% of particles are presented in Table 3. There is an increase in the measured hardness and reduced modulus of elasticity with the increase of BSO particles content, as was expected [95, 100]. The reduced modulus for composite with 0.5 wt% of BSO increased by2.5 % and the hardness by 4.6 % in comparison to the neat PMMA films. For composites with 1.0 wt % of BSO modulus increases by about 16.6 % and hardness increase is around 34 %.

Table 3 Nanoindentation tests results

C_{BSO}, wt%	$\boldsymbol{E_r}$, GPa	Standard deviation,GPa	H, GPa	Standard deviation,GPa
0.0	4.685705	± 0.34	0.281594	± 0.018
0.5	4.802341	± 0.25	0.294626	± 0.026
1.0	5.464252	± 0.45	0.377017	± 0.035

SYNTHESIS AND CHARACTERISATION OF FLUORESCENT POLYMER NANO TO MICROFIBERS

EXPERIMENTAL

Commercially available pellets of PMMA Acryrex® CM205 (Chi Mei Corp.) ($M_w \approx 90400$ g mol^{-1}) were used as the matrix for preparing samples by using dimethylformamide (DMF, anhydrous, 99.8%, Sigma-Aldrich) as solvent and laser dye RhB (Sigma-Aldrich, M = 479.01 g mol^{-1}) was chosen for the incorporation in the polymer matrix. The aim of starting experiments was to establish the conditions of PMMA fiber electrospinnig. Homogenous solutions of polymer were obtained by stirring for 48 h by the magnet mixer at room temperature. The concentrations of PMMA in DMF solutions were 6 wt% and 22 wt% according literature data [24]. The electrospinning was performed on Electrospinner CH-01, Linari Engineering, Italy. A plastic syringe (20 ml) with a metallic needle of 1 mm inner diameter was set vertically on the syringe pump (R-100E, RAZEL Scientific Instruments) and the high-voltage power supply (Spellman High Voltage Electronics Corporation, Model: PCM50P120) was set to a voltage of 28 kV. The distance of the needle tip from the collector was 15 cm and flow rate was different (5 ml/s, 1 ml/s and 0.5 ml/s). Electrospun fibers were dried for 8 hours at 50°C in a vacuum dryer oven. The morphology of nanofibers was obtained using a Field Emission Scanning Electron Microscope (FESEM, TESCAN MIRA 3) with fracture surfaces sputtered with gold. SEM analysis revealed that the best results were achieved with a 22 wt% solution of PMMA in DMF at a flow rate of 0.5 ml h^{-1}. For this reason, it was decided to use this set of parameters to continue the experiments with RhB doped PMMA.

For the production of RhB doped PMMA fibers the procedure for solutions was similar. Homogenous solutions of polymer were obtained by stirring for 48 h by the magnet mixer at room temperature and after dissolution of the polymer; the dye was directly added to the solution and mixed for a further 10 min. The contents of RhB in the PMMA were 0.05 wt%, 0.1 wt%, 0.2 wt%, 0.5 wt%, 1.0 wt% and 2.0 wt% after the

evaporation of the solvent. Rheological behavior of PMMA dye solutions was analyzed by using Discovery Hybrid Rheometer HR2 (TA instruments) with parallel plate (diameter 25 mm; gap 500 μm) geometry at 25 °C. Flow characteristics (steady-shear measurements) of the samples were measured by varying the shear rate from 1 to 2000 1/s.

The electrospinning process was setup as in previous experiments: an applied voltage was 28 kV, the flow rate of polymer solution was constant at 0.5 ml h^{-1} and the distance of the needle tip from the collector was 15 cm. All samples were obtained at 20 °C and 30% air humidity. The obtained nanofibers were dried in vacuum oven 20 h at 80ºC.

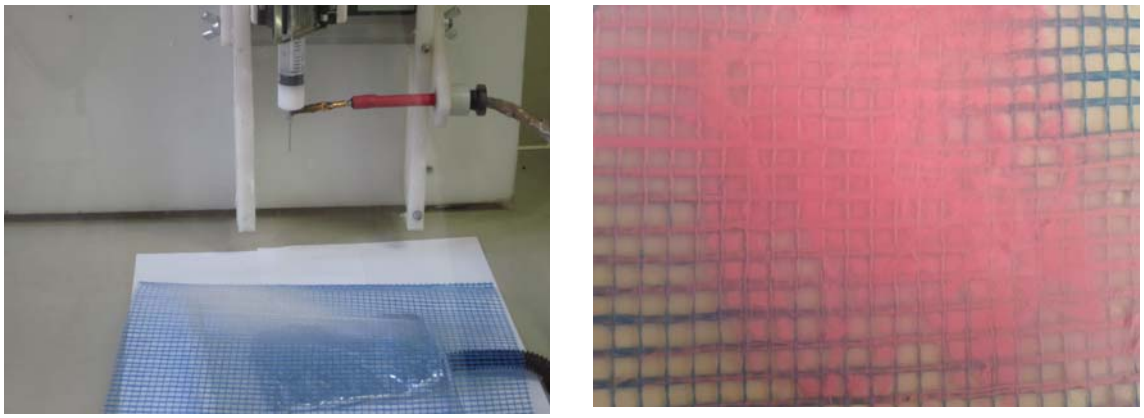

a) b)

Figure 39 a) Electrospinning setup, b) Electrospun nanofibers on the grid

The infrared (IR) spectra of samples in KBr discs were obtained by transmission Fourier transform infrared (FTIR) spectroscopy (Hartmann & Braun, MB-series). The FTIR spectra were recorded between 4000 and 400 cm^{-1} with a resolution of 4 cm^{-1}.

The diameter of the electrospun nanofibers was measured by Image Pro Plus 4.0 (100 measuring per photo). Differential scanning calorimetry (DSC) measurements were conducted using a TA Instruments, TA DSC Q10 instrument calibrated to indium standards. The samples mass of 0.5 mg were investigated. The measurements were performed under a dynamic nitrogen flow of 50 ml min^{-1} in the temperature range from 30 °C to 155 °C. The samples were heated up to 155 °C at a rate of 10 °C min^{-1}, kept at 155 °C for 5 min to erase thermal history and then cooled to 30 °C at the same rate. A

second heating was performed on the each sample. The glass transition temperature was determined at the midpoint of the initial slope change.

The basic setup of the time-resolved laser-induced fluorescence measurement system consisted of an Nd-YAG Vibrant OPO laser system and a Hamamatsu streak camera. The output of the OPO could be continuously tuned over a spectral range from 320 nm to 475 nm. After analysis of the preliminary results, for measurements presented herein, the second harmonic of the Nd-YAG laser, 532 nm, was used as an excitation source of the samples. The wavelength of 532 nm is closer to the absorption peak of Rh B than the OPO output. The emission spectra were recorded using a streak scope (Hamamatsu model C4334-01) with the integrated video streak camera. The fluorescence emission was collected at 90° from the excitation and dispersed by a 0.3 m focal length triple grating imaging spectrograph (SpectraPro-2300i). A grating of 50 g mm^{-1} was used to cover a 330 nm spectral range.

RESULTS AND DISCUSSIONS

Electrospinning parameters

In starting experiments of electrospinning of PMMA solutions the three kinds of nanofibers morphologies obtained as: ringlike particles, bead-like nanofibres and ultrafine nanofibres. As shown in Fig. 40a, bead-like nanofibres are fabricated from 22 wt% PMMA in DMF with a flow rate of 5 ml h^{-1}. The ringlike morphology (Fig. 40b) was obtained from 6 wt% PMMA in DMF with a flow rate of 1 ml h^{-1}. Electrospinning at relatively low polymer concentrations results in particles rather than fibers [101]. It is obvious that the jet of polymer solution from the tip of a capillary begins to break up into droplets at lower polymer concentration. The solution viscosity should be above a minimum for fiber formation, if the viscosity is too low, the process results in electrospraying to yield vesicles under the influence of an electric field. The smooth, bead –free nanofibers were produced by a combination of higher concentration and lower rate (a 22 wt% solution of PMMA in DMF at a flow rate of 0.5 ml h^{-1}). For this

reason, it was decided to use this set of parameters to continue with the experiments in which PMMA fibers doped with RhB were fabricated.

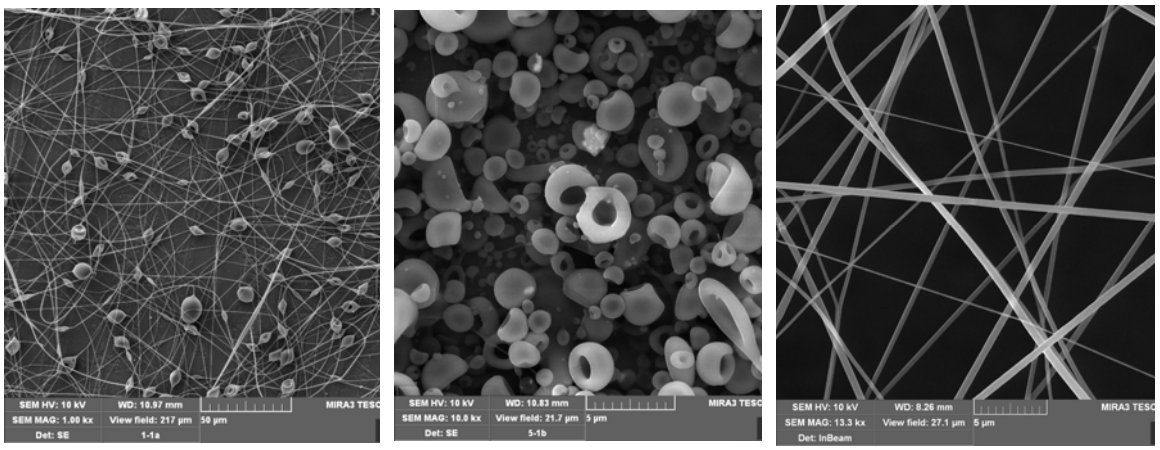

a) b) c)

Figure 40 FESEM photographs of a) PMMA in DMF, flow rate 5 ml h^{-1} (22 wt%); b) PMMA in DMF, flow rate 5 ml h^{-1} (6 wt%); c) PMMA in DMF, flow rate 0.5 ml h^{-1} (22 wt%).

Viscosity of solutions and morphology of nanofibers

The viscosities of solutions (measurements at shear rate 100 s^{-1}) with various Rh B concentrations used are listed in Table 4 and dependence of viscosity on the shear rate is presented on Figure 41. FESEM photographs of PMMA –Rh B nanofibers are presented in Figures 42-48. Image analysis revealed that nanofibers were beads-free and with a smooth surface. These fibers presented regular surface morphologies.

Figure 49 presented dependence of fiber diameter on the content of Rh B. During the electrospinning process, the polymer solution would be drawn from the nozzle of the spinneret and the electrical properties of the solution, namely, viscosity and surface tension will determine the extent of stretching of the solution under electrostatic forces. The smaller diameter of the nanofibers from the lower viscosity is the result of the

solution being stretched easily during electrospinning. The larger nanofiber diameters are attributed to the viscosity of the solution that was high enough to lower the bending instability of the jet. The solution becomes resistant to stretching by the electrical charges on the electrospinning jet. From the Table 4 it is obvious that fiber diameter decreased as the viscosity of solution decrease from pure PMMA to the 0.05 wt% Rh B doped PMMA. After that value the change in viscosity was in the range of 10%, but the diameter of nanofibers continually decreased. The explanation for that behavior could be the change in solution conductivity. RhB am a polar dye belongs to the xanthine family and it is easily dissolved in polar solvents, like DMF. Depends on the pH, Rh B exists in a number of possible molecular forms such as cationic, zwitterionic, quinonic and lactonic [64]. Since the ionic charges have a direct relation with the electrical conductivity of the solution, increases the charge density on the surface of the ejected jet, leading to an increase in the electric charges carried by the jet. When the conductivity of the solution is increased more charges can be carried by the jet. An increase in the conductivity means that electrostatic forces can now overcome the surface tension much easier [101, 102] As a result, when the charge density increases in the jet, more stretching and elongation of the jet takes place during electrospinning, and thereby causing a reduction in fiber diameter.

The fiber diameter decreased from 1395 ± 262 nm for pure PMMA to 598 ± 115 nm for PMMA doped with 1.0 wt% Rh B. The distribution of fiber diameter followed the same trend, the standard deviation decreased from 362 nm for pure PMMA to 98 nm, and after that concentration rose. These results indicated that for concentration of Rh B about 0.5-1.0 wt% the behavior of solution has been changed.

Table 4. Viscosity of solutions and diameter of electrospun nanofibers from Image analysis

Concentration of RhB, wt%	*Viscosity, Pas*	*Mean diameter of fibers, nm*
0	2.23	1395 ± 262
0.05	1.75	1068 ± 306
0.1	1.72	967 ± 258
0.2	1.80	650 ± 90
0.5	1.90	743 ± 98
1.0	1.72	598 ± 115
2.0	1.82	623 ± 112

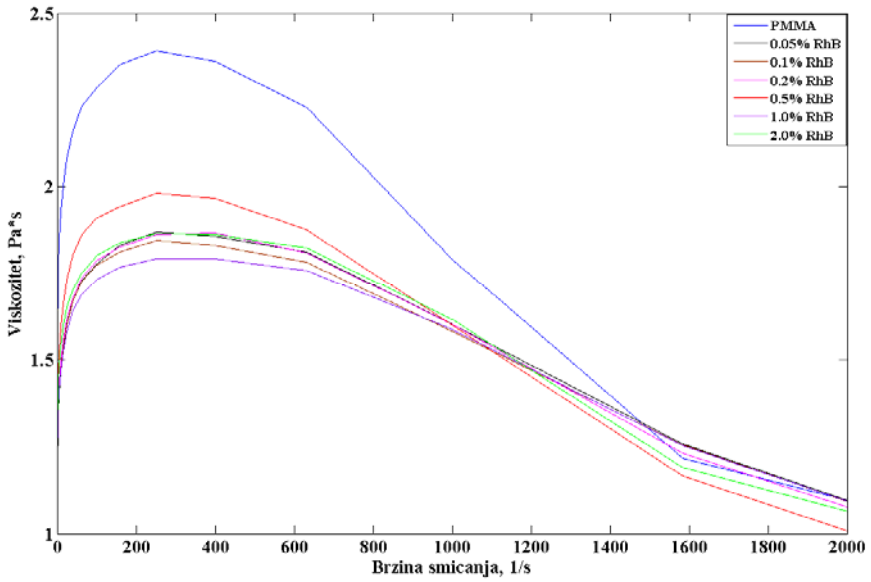

Figure 41 Dependence of viscosity on the shear rate

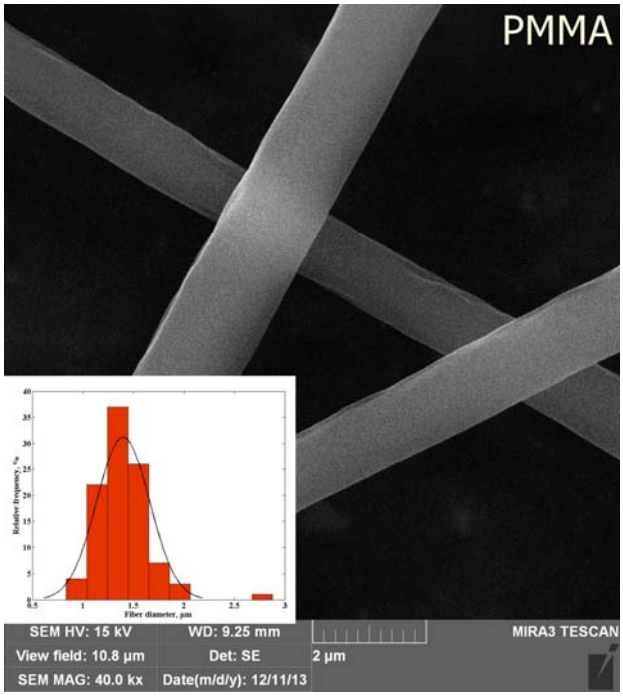

Figure 42 FESEM photograph of PMMA nanofibers and results of Image Analisys

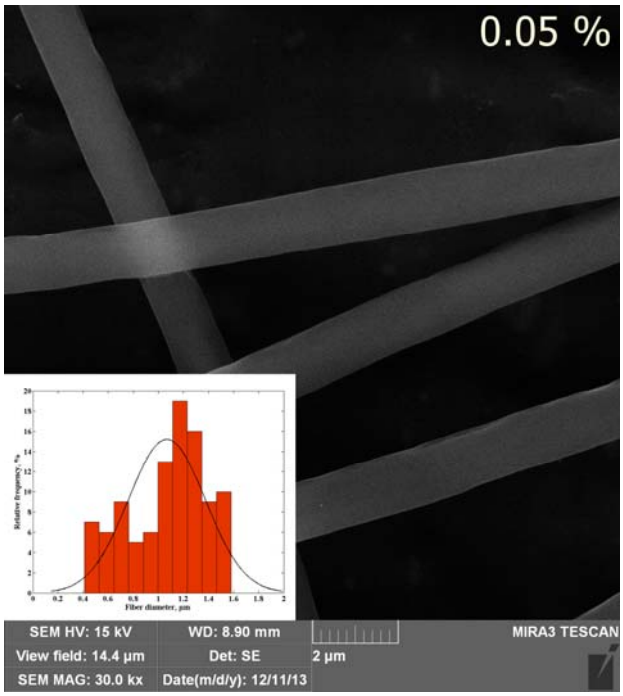

Figure 43. FESEM photograph of PMMA-0.05 wr % RhB nanofibers and results of Image Analisys

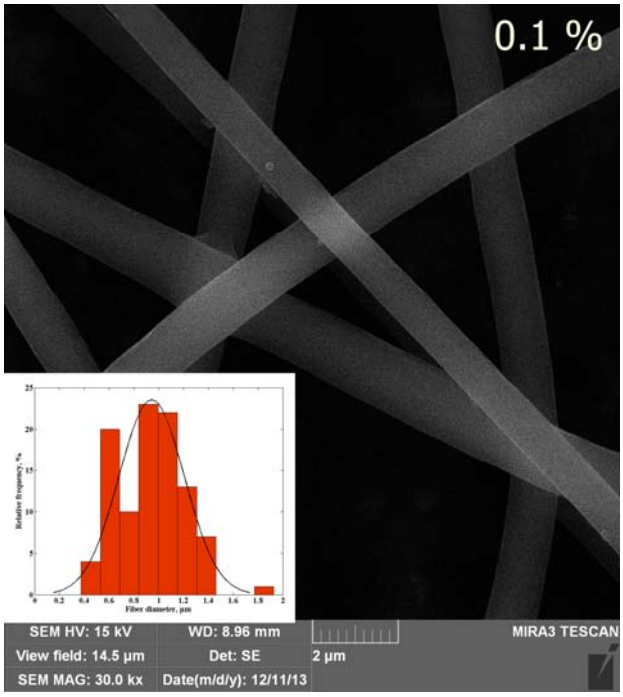

Figure 44 FESEM photograph of PMMA-0.1 wt % RhB nanofibers and results of Image Analisys

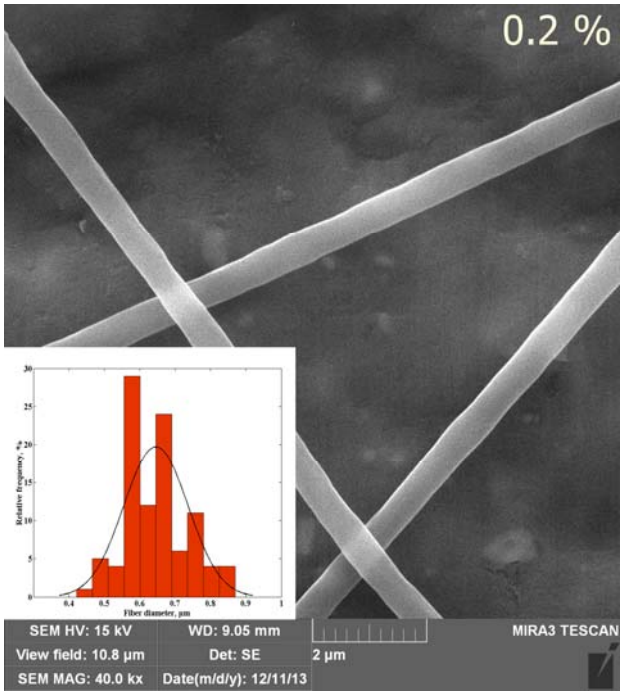

Figure 45. FESEM photograph of PMMA-0.2 wt % RhB nanofibers and results of Image Analisys

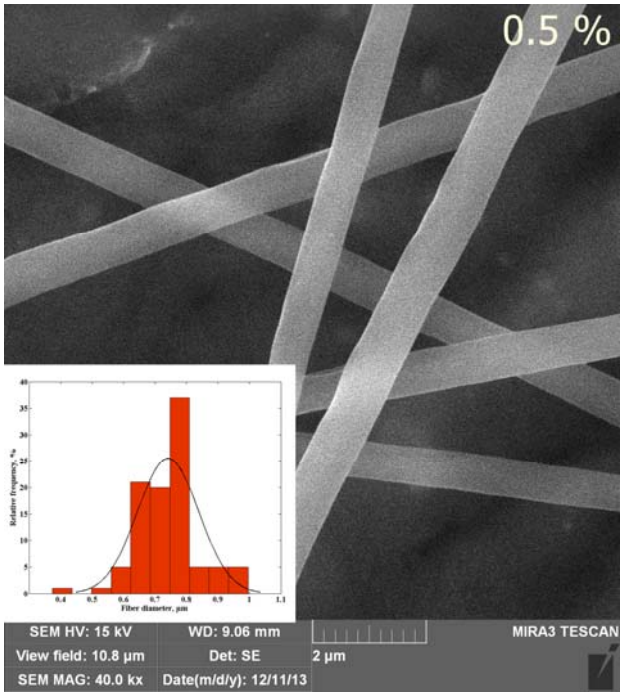

Figure 46 FESEM photograph of PMMA-0.5 wt % RhB nanofibers and results of Image Analisys

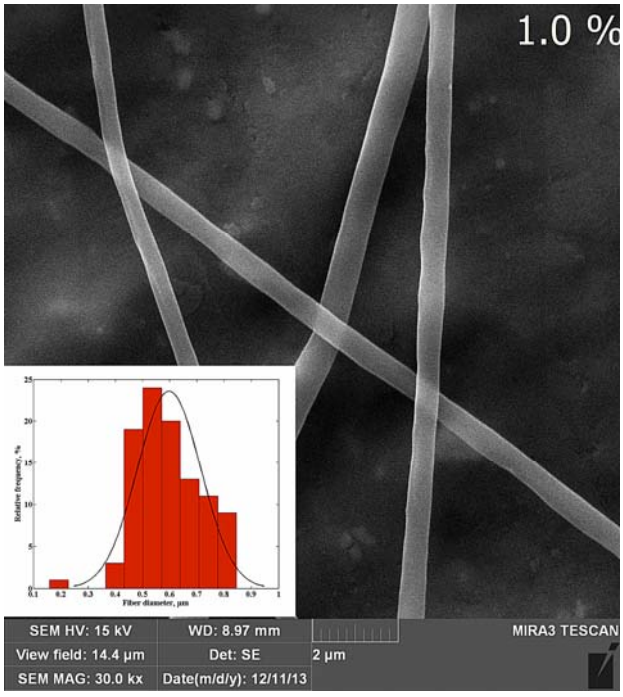

Figure 47. FESEM photograph of PMMA-1.0 wt % RhB nanofibers and results of Image Analisys

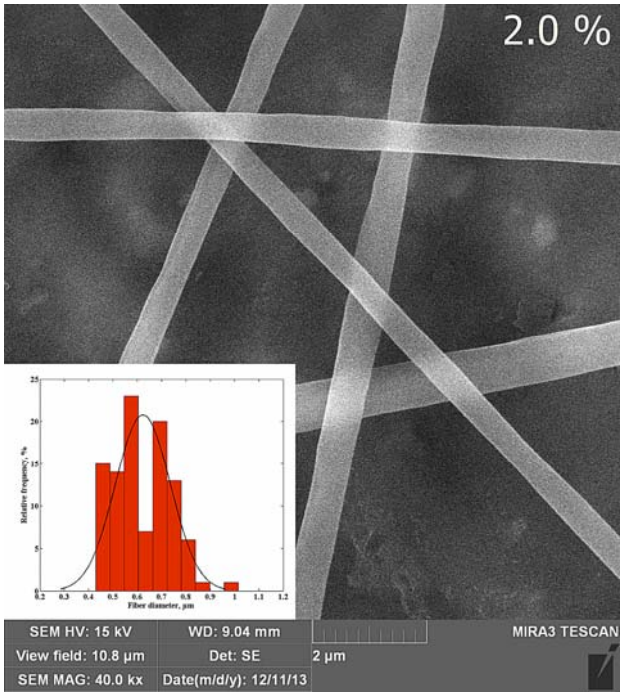

Figure 48. FESEM photograph of PMMA-2.0 wt % RhB nanofibers and results of Image Analisys

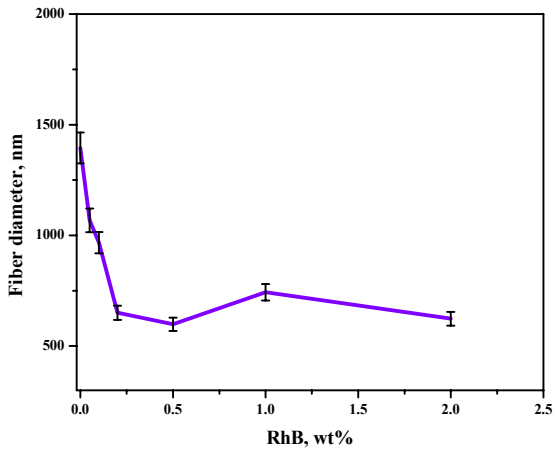

Figure 49 Dependence of the fiber diameter on the content of Rhodamine B

FTIR spectrum

The FTIR spectra of pure poly (methyl methacrylate) (PMMA) fibers (spectrum a) and RhB (spectrum b) are presented in Fig. 50.

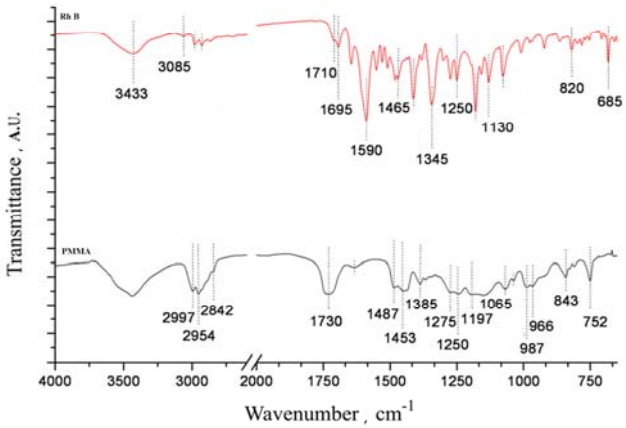

Figure 50 a) FTIR spectra of a) poly(methyl methacrylate) fibers and b) RhB

Spectrum a) exhibits vibrational bands typical for PMMA, *i.e.*, vibrational bands at 987 and 1453 cm^{-1} that belong to O-CH_3 bending and stretching deformation of PMMA, respectively, bands at 1730 and 1250 cm^{-1} that are assigned to stretching of C=O groups, a band at 1065 cm^{-1} that could be ascribed to the C-O stretching vibration and a band at 1197 cm^{-1} that belongs to the skeletal chain vibration. The other bands appearing in the 3000 – 2800 cm^{-1}, 1490 – 1275 cm^{-1} and 900 – 750 cm^{-1} spectral regions correspond to different CH_3 and CH_2 vibrational modes [104, 105].

In spectrum b, vibrational bands corresponding to RhB can be seen. Namely, a broad intensity band at 3433 cm^{-1} is associated with the O-H stretching vibration of hydroxyl groups. Its appearance is attributed to absorption of water by the material. A weak intensity band at 3085 cm^{-1} belongs to aromatic C-H vibrations, which also appear at 1130 cm^{-1} (plane bending), 820 cm^{-1} (out of plane bending) and at 685 cm^{-1} (wagging vibrations). In addition, the band at 1710 cm^{-1} belongs to the C=N stretching vibration,

while the band at 1695 cm^{-1} is associated with C=O stretching. A sharp absorption band appearing at 1590 cm^{-1} is assigned to the asymmetric stretching vibration of the COO^- group, the presence of which is further confirmed by the occurrence of a band at 1465 cm^{-1} ascribed to the symmetric stretching of the group. The aromatic skeletal C–C stretch and C–O stretch can be observed at 1345 and 1250 cm^{-1}, respectively [105, 106].

The FTIR spectra of PMMA fibers doped with different concentrations of the RhB, *i.e.*, 0.5, 1 and 2 %, are presented in Fig. 51. The overall analysis of the spectra revealed that after the introduction of RhB in the PMMA fibers, the vibrational bands became more intense and their shape sharpened compared to of the corresponding bands of pure PMMA fibers. Moreover, due to the presence of the RhB, the vibrational bands in the 3000–2800 cm^{-1} and 1750 – 1400 cm^{-1} spectral regions were slightly shifted towards lower wavenumbers. Namely, these changes were the most visible in the case of the vibrational band at 1730, characteristic for the stretching of the C=O of PMMA fibers, which was strongly increased and insignificantly blue-shifted to the wavenumber 1728 cm^{-1} after doping of the PMMA fibers with RhB. Since the band at 1695 cm^{-1} associated with C=O stretching of the pure RhB (Fig. 50b) does not appear in the spectra of PMMA doped with RhB (Fig. 51), the existence of such a strong band at 1728 cm^{-1} could be attributed to the mutual vibrations of the C=O groups in the structure of PMMA fibers doped with RhB. In addition, the vibration of C=N groups of the RhB, found at 1710 cm^{-1}, could also produce a slight shift of the band from 1730 to 1728 cm^{-1}.

Detailed inspection of the IR spectra of PMMA fibers doped with RhB also revealed the formation of new vibrational bands of rather weak intensities, appearing at 1590, 912 and 828 cm^{-1}. While the latter two could be attributed to the C-H vibration of the aromatic ring of RhB [104]., the appearance of the band at 1590 cm^{-1}, characteristic for the COO^- vibrations, confirms that RhB did not react with the functional groups of PMMA. By appearance of these peaks, the presence of RhB molecules within the PMMA matrix has been confirmed, implying that the RhB is not chemically bonded but rather physically embedded within the PMMA matrix [50].

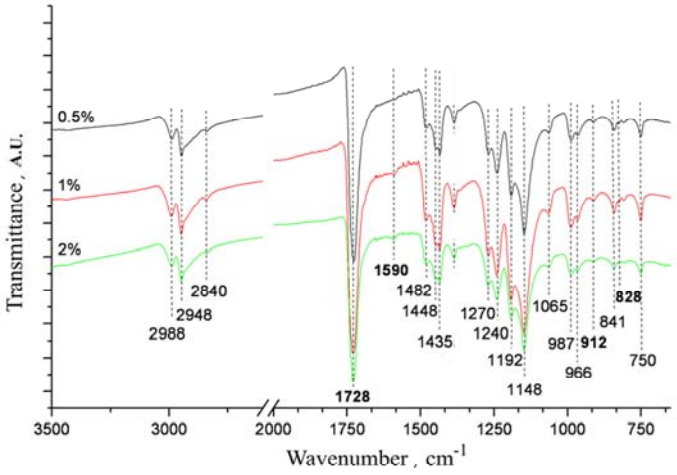

Figure 51 FTIR spectra of poly(methyl methacrylate) fibers doped with different concentrations of RhB.

The results of DSC analysis are given in the Figure 52. The analyses were realized for pure powder PMMA, PMMA nanofibers and PMMA – Rh B nanofibers of different composition. The values of T_g and $\Delta C_P/\Delta T$ are marked. The powder of PMMA shows T_g at 113.53ºC. It can be affirmed that the PMMA–solvent interaction is stronger, because the PMMA nanofibers electrospun from DMF solution at 114.71 ºC. The introduction of the Rh B in polymer shift T_g to higher values up to**.**

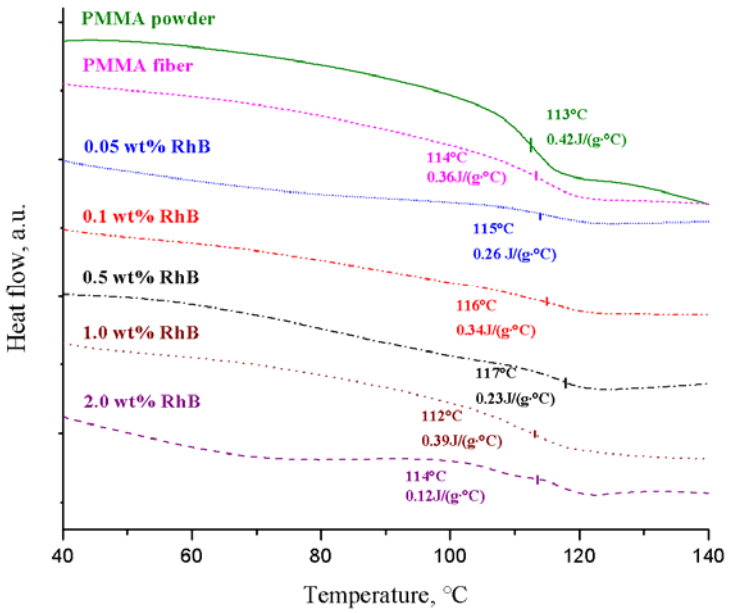

Figure 52 DSC analysis of a) PMMA film; b) PMMA nanofibers; c) PMMA - 2 wt% RhB film and c) PMMA- 2 wt% RhB nanofibers

a concentration of 0.5 wt% (117.14 ºC), and shows decrease beyond that concentration. This is correlated to the viscosity/polarity-dependent behavior of Rh B molecules in solvent [107-109]. This is also accorded with the determined viscosity of solutions with different concentration of Rh B. Having smaller dye–dye molecular distances, Rh B in DMF permit the formation of aggregates which are responsible for the reduction of Tg in fiber with higher content of Rh B.

Fluorescence response

A typical streak image of the fluorescence response of the fibers is shown in Fig. 53. The streak images acquired in gray scale are presented in pseudo-color, where different intensities are coded as different colors. The images were acquired in the photon counting mode operation; thus, intensity corresponds to the number of counting photons. Wavelength scale (horizontal) is in the range between the 465 nm and 795 nm. Timescale (vertical) is about 50 ns. Laser excitation at 532 nm is also visible on the image. After deconvolution of the laser profile from the fluorescence response profile (green curve), an RhB fluorescence lifetime of about 3 ns was obtained, and this is in agreement with published values [109-110].

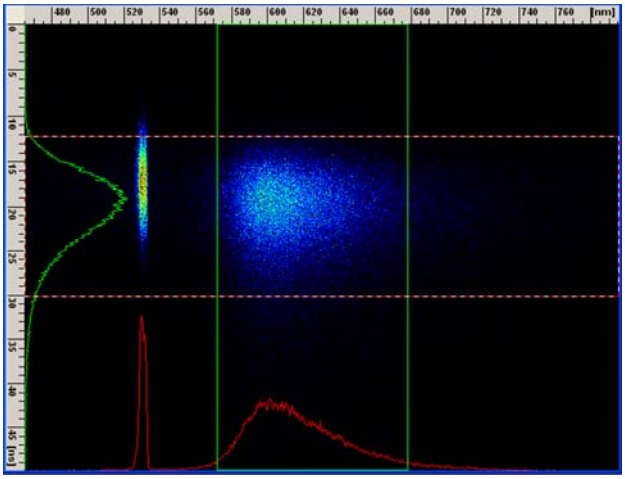

Figure 53 A streak image of the fluorescence response of the PMMA- 0.5 wt% RhB fibers.

The fluorescence emission spectrum of the fibers is shown in Fig. 54. A shift of the fluorescence peak towards higher wavelengths could be noticed with increasing concentration of Rhodamine B. Increasing the concentration of the dye resulted in a red shift in the fluorescence wavelength to higher wavelengths as can be seen in Fig. 55, which shows the dependence of the wavelength of maximum emission on the concentration of Rh B in PMMA. These results are in agreement with the literature [95,111]. It can also be noticed that the plateau had not been reached yet [110]. When

the plateau is reached, at high concentrations, aggregation formation restricts the peak shift.

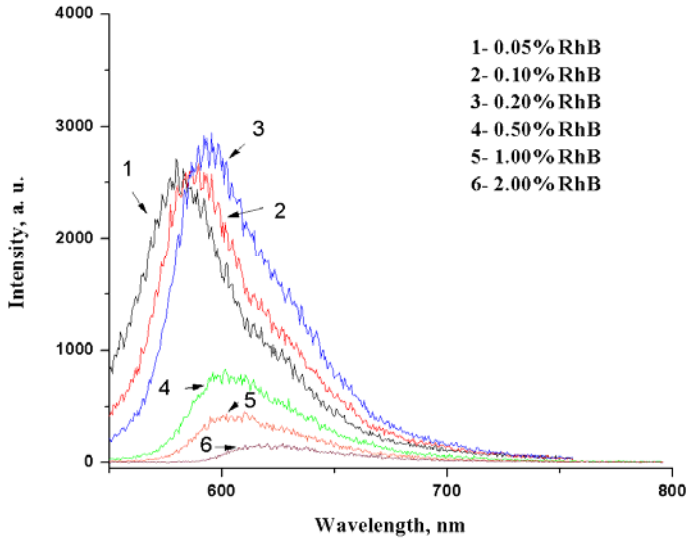

Figure 54 Emission fluorescent spectra of nanofibers with different contents of Rhodamine B.

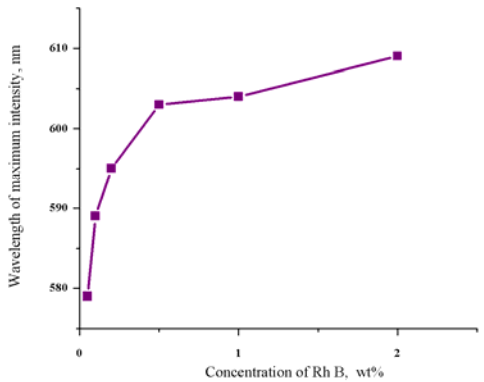

Figure 55 Dependence of the wavelength of the maximum emission intensity on the content of Rhodamine B.

The intensity of the fluorescence emission peak increased with concentration of RhB until 0.2 wt% and later, at higher concentrations, it decreased and became broader, which is in agreement with published results for RhB in solution and PMMA films [95, 110]. This is correlated to the viscosity/polarity-dependent nonradioactive deactivation processes in Rh B.

The emission spectra of films and corresponding nanofibers are presented on figure 56. It is obvious that intensity of emission spectra of films is higher than for nanofibers. There is the trend of peak for composite with higher content of Rh B – decreasing of peak intensity with raised content of Rh B. Also, the peaks of films are shifted toward higher wavelengths.

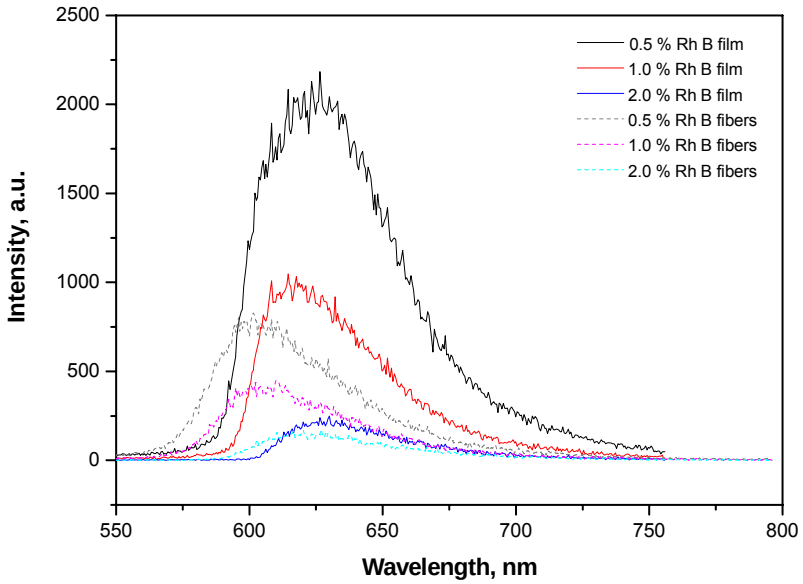

Figure 56 Fluorescence spectra of films and nanofibers of RhB doped PMMA

CONCLUSION

The study evaluated influence of the addition of heavy BSO powder to PMMA matrix. The single crystal structure $Bi_{12}SiO_{20}$ was confirmed by XRD. FTIR characterization identified BSO crystals in the composite and showed that no other bounds were created during the processing. The characterization of the composite revealed that the thermal and mechanical properties were improved with addition of BSO powders. Raman spectra showed that particles have retained their optical activity after implementation in the polymer matrix. Value of refractive index of composites was higher then for neat PMMA and increased with the powder content. Tensile testing showed, as compared to the matrix, an increase of the initial modulus and the tensile strength. Nanoindentation revealed that hardness and reduced modulus of elasticity have shown significant increase with raised particles content.

These results indicate that the crystalline BSO particles are useful fillers to simultaneously increase both refractive index and mechanical properties of polymer composites. Presented results show good potential of PMMA-BSO composites to be used in scintillating systems mostly in the field of light emitting devices, waveguide devices, also in photovoltaic modules and sensors.

Electrospinning of PMMA doped with different contents of RhB was performed. Examination of the morphology of the fibers revealed beads-free nanofibers with smooth surface and the mean diameter of nanofibers decreases with increasing content of RhB in PMMA. After addition of RhB in the PMMA, the T_g of increased with Rh B content up to a concentration of 0.5 wt%. The fluorescence response of fibers after laser excitation indicated that emission peak increased with concentration of RhB until 0.2 wt%. The fluorescence emission intensity of RhB becomes broader and shifted to higher wavelength with increasing RhB concentration in the nanofibers. The values of solutions viscosity, T_g and fluorescence emission peak indicated that there is a

significant and critical concentration of Rh B (0.2 wt%- 0.5 wt %), and beyond these values change according viscosity/polarity behavior.

Scintillating composites can find many potential applications due to their low cost and ease of preparation, high density and efficiency, size and compactness compared to other scintillation counters.

These composites could be used for a variety of applications which include gamma-ray spectroscopy, contamination surveys, land surveys and aerial radiological surveys for the presence of gamma- emitting radio nucleides. They can be used as detectors for safety detector requirements like in a scanner to rapidly identify a suspect luggage in a few cubic meter large container moving across the inspection device and remote detection of fissile materials These detectors can be used for laboratory applications, such as nuclear material processing, laboratory research activity, to field applications such as nuclear waste processing and management, nuclear explosion monitoring, maritime security and radioactive material transportation monitoring.

Scintillating composite fibers could find applications in medical imaging techniques, where a radioisotope is injected into the body, which produces ionizing radiation that can be detected by inserting a scintillating fiber sensor into the diseased part. Scintillating fibers can also be used in the form of an array for imaging purposes in order to determine something about the physiology or anatomy of the target organ.

REFERENCES

1. Z.L. Wang, Z.C. Kang, Functional and Smart Materials Structural Evolution and Structure Analysis, first ed., Plenum Press, New York, 1998.
2. D.R. Paul, L.M. Robeson, *Polymer* 49 (2008) 3187-3204.
3. S.C. Tjong, *Mater. Sci. Eng*. R 53 (2006) 73-197.
4. Y. Long, R.A. Shanks, *J. Appl. Polym. Sci*. 62 (1996) 639-646.
5. Z. Bartczak, A.S. Argon, R.E. Cohen, M. Weinberg, *Polymer* 40 (1999) 2347-2365.
6. R.K.D. Misra, P. Nerikar, K. Bertrand, D. Murphy, *Mater Sci Eng* A 384 (2004) 284-298.
7. H. Unal, A. Mimaroglu, M. Alkan, *Polym Int.* 53 (2004) 56-60.
8. H.R. Allcock, J.D. Bender, Y. Chang, *Chem. Mater*. 15 (2003) 473-477.
9. C. Lü, B. Yang, *J. Mater. Chem.* 19 (2009) 2884–2901.
10. E. Ritzhaupt-Kleissl, J. Böhm, J. Hauβelt, T. Hanemann, *Adv. Eng. Mater.* 7 (2005) 540-545.

11. G.I. Britvich, I.G. Britvich, V.G. Vasil'chenko, V.A. Lishin, V.F. Obraztsov, V.A. Polyakov, A.S. Solovjev, V.D. Ryzhikov, *Nucl Instrum Methods Phys Re*s A 469 (2001) 77-88.

12. I.M. Radović, D.B. Stojanović, P.S. Uskoković, S.N. Kostić, M.M. Jakovljević, V.J. Radojević, R.R. Aleksić, 49th Meeting of the Serbian Chemical Society Proceedings, Kragujevac 2011 103-106.

13. P.P. Kiran, S.V. Rao, M. Ferrari, B.M. Krishna, H. Sekhar, S. Alee, D.N. Rao, *Quantum Optics* 40 (2010) 223–234.

14. R.C. Fernow, Introduction to experimental particle physics, Cambridge University Press, Cambridge, 1986.

15. N. Akchurin, F. Bedeschi, A. Cardini, M. Cascella, G. Ciapetti, D. De Pedis, M. Fasoli, R. Ferrari, S. Franchino, M. Fraternali, G. Gaudio, J. Hauptman, M. Incagli, F. Lacava, L. La Rotonda, S. Lee, M. Livan, E. Meoni, A. Negri, D. Pinci, A. Policicchio, F. Scuri, A. Sill, G. Susinno, T. Venturelli, C. Voena, R. Wigmans, *Nucl Instrum Methods Phys Res* A 640 (2011) 91-98.

16. A. Golubović, S. Nikolić, R. Gajić, S. Đurić, A. Valčić, *J.Serb.Chem.Soc.* 67 (2002) 279-289.

17. S. Nikolić, A. Valčić, V. Radojević, Proc. XLI Yugoslav Conference ETRAN, Zlatibor, Serbia, vol. 4, 1997, 457-459

18. J.-C. Chen, L.-T. Liu, C.-C. Young, *J Cryst Growth* 198/199 (1999) 476-481.

19. I. Kusachi, C. Henmi, *Japan. Miner J* 15 (1991) 343-348.

20. H.J. Tiziani, F. Höller, Proceedings of the International Topical Meeting on Image Detection and Quality, Paris, France, 1986.

21. L. Escobar-Alarcón, E. Haro-Poniatowski, M. Fernández-Guasti, A. Perea, C.N. Afonso, T. Falcón, *Appl. Phys.* A 69 (1999) 949-952.

22. R.N. Panda, A. Pradhan, *Mater Chem Phys* 78 (2002) 313-317.

23. G. González, A. Zúñiga, L. F. Magaña,. *Rev. Mex. Fis.* 54 (2008) 433-439.

24. J. Potter, R.C. Spooncer, P.R. Hobson, Proceedings of SPIE. 1732(1993): 470-480

25. A. Veber, Š. Kunej, D. Suvorov, *Ceram Inter* 36 (2010) 245-250.

26. J. -K. Chen, S. -W. Kuo, H. -C. Kao, F. -C. Chang, *Polymer,* Vol. 46 (2005) 2354

27. D.K. Platt, Engineering and High Performance Plastics Market Report, Rapra Technology Limited, Shawbury, Shrewsbury, Shropshire, SY4 4NR, UK., 2003.

28. M.T. Santos, L. Arizmendi, D. Bravo, E. Diéguez, *Mater Res Bull* 31 (1996) 389-396.

29. I.F. Vasconcelos, M.A. Pimenta, A.S.B. Sombra,. *J. Mat. Sci.* 36 (2001) 587-592.

30. [M. Dixit, S. Gupta, V. Mathur, K. S. Rathore, K. Sharma, N. S. Saxena, *Chalcogenide Lett,* Vol. 6, No. 3, (2009) 131-136.

31. P. Moy, C.A. Gunnarsson, T. Weerasooriya, W. Chen, Stress-Strain Response of PMMA as a Function of Strain-Rate and Temperature, in: T. Proulx (Ed.), Dynamic Behavior of Materials, Volume 1, Conference Proceedings of the Society for Experimental Mechanics Series 99, The Society for Experimental Mechanics, Inc., Springer Science+Business Media, New York, 2011, pp. 125-133.

32. M.M. Nasseri , Q. Ma , Z. Yin , D.M. Zhu, *Nucl Instrum Methods Phys Re*s B 234 (2005) 362–368

33. Y. Xia, P. Yang, Y. Sun, Y. Wu, B. Mayers, B. Gates, **Y**. Yin, F. Kim, H. Yan, *Adv. Mater*. **5** (2003) 353

34. C. M. Lieber, *MRS Bull*. **287** (2003) 486

35. C. H. Wang, Y. Q. Dong, K. Sengothi, K. L. Tan, E. T. Kang, *Synth. Met.* **1021–3** (1999) 1313

36. W. J. Li, C. T. Laurencin, E. J. Caterson, R. S. Tuan, F. K. Ko, *J. Biomed. Mater. Res*. **604** (2002) 613
37. X. Y. Wang, C. Drew, S. H. Lee, K. J. Senecal, J. Kumar, L. A. Samuelson, *Nano Lett.* **2** (2002) 1273
38. J. S. Kim, D. H. Reneker, *Polym. Compos*. **201** (1999) 124
39. S. Jiang, G. Duan, H. Hou, A. Greiner, S. Agarwal, *ACS Appl. Mater. Interfaces* **4** (2012) 4366
40. N. Tomczak, S. Gu, M. Han, N. F. van Hulst, G. J. Vancso, *Eur. Polym. J.* **42** (2006) 2205
41. Y. Shen, P. N. Prasad, *Appl. Phys. B* **74** (2002) 641
42. H. Q. Yu, B. J. Li, *Sci. Rep.* **3** (2013) 1674
43. R. Dersch, M. Steinhart, U. Boudriot, A. Greiner, J. H. Wendorff, *Polym. Adv. Technol*. **16** (2005) 276
44. K. J. Lee, J. H. Ho, Y. Kim, J. Jang, *Adv. Mater.* **18** (2006) 2216
45. A. Noy, A. E. Miller, J. E. Klare, B. L. Weeks, B. W. Woods, J. J. De Yoreo, *Nano Lett.* **2** (2002) 109
46. F. Quochi, F. Cordella, A. Mura, G. Dongiovanni, F. Balzer, H.-G. Rubahn, *Appl. Phys. Lett.* **88** (2006) 041106
47. H. Yu, Baojun Li, *Sci. Rep.* **3** (2013) 1674
48. D. Pisignano, G. Maruccio, E. Mele, L. Persano, F. Di Benedetto, R. Cingolani, *Appl. Phys. Lett.* **87** (2005)123109
49. A. Formhals, US Patent 2,116,942 (1938)
50. C. Y. Hsu, Y. L. Liu, *J. Colloid Interface Sci.* **350** 1 (2010) 75
51. A. G. Kanani, S. H. Bahrami, *Trends Biomater. Artif. Organs* **24** (2010) 93
52. D. H. Reneker, I. Chun, *Nanotechnology* **7** (1996) 216
53. R. Jaeger, H. Schonherr, G. J. Vancso, *Macromolecules* **29** (1996) 7634
54. M. Bognitzki, W. Czado, T. Frese, A. Schaper, M. Hellwig, M. Steinhart, *Adv Mater* **13** (2001) 70
55. S. Schlecht, S. Tan, M. Yosef, R. Dersch, J. H. Wendorff, Z. Jia, A. Schaper, *Chem. Mater.* **17** (2005) 809
56. X. Wang, S.-H. Lee, B.-C. Ku, L. A. Samuelson, J. Kumar, *J. Macromol Sci A* **39 (**2002) 1241

57. J. L. Davis, K. Guzan, K. Mills, L. Han, *Proceedings of NSTI-Nanootech 2010* Nanotechnology Anaheim, California, USA 2010, p. 769
58. A. Tagaya, Y. Koike, T Kinoshita, E. Nihei, T. Yamamoto, K. Sasaki, *Appl. Phys. Lett.* **63** (1993) 883
59. G. Somasundaran, A. Ramalingam, *Opt. Laser Technol* **31** 5 (1999) 351
60. H. Liang, Z. Zheng, Z. Li, J. Xu, B. Chen, H. Zhao, Q. Zhang, H. Ming, *J. Appl. Polym. Sci.* **93** (2004) 681
61. K. Geetha, M. Rajesh, V. P. N. Nampoori, C. P. G. Vallabhan, P. Radhakrishnan, *J. Opt. A: Pure Appl. Opt.* **6** (2004) 379
62. P. Kumar, D. R. Bajpai. M. Keller, *Microsyst Technol* **14** (2008) 1165
63. G. Sreekumar, P. G. Louie Frobel, S. Sreeja, S. R. Suresh, S. Mayadevi, C. I. Muneera, C. S. Suchand Sandeep, R. Philip, C. Mukharjee, *Chem. Phys. Lett*. **506** (2011) 61
64. M. Fikry, M. M. Omar, L. Z. Ismail, *J. Fluoresc*. **19** (2009) 741
65. Piotr A.Rodnyi, "Physical Processes Inorganic Scintillators," CRC Press, 1997
66. Paul lecoq, Alexander Annenkov, Alexander Gektin, Mikhail Korzhik, Christian Pedrini, "Inorganic Scintillators for Detector Systems," Physical Principles and Crystal Engineering, Springer 20006
67. Glenn F. Knoll, "Radiation Detection and Measurement," John Wiley & Sons, 1989
68. J.B. Kirks, "Scintillation Counters," McGraw Hill Book Co., Inc, 1953
69. A. Jayaprakash, Innovative scintillating optical fibers for detecting/monitoring gamma radiation, Master thesis, Faculty of Mississippi State University, 2006
70. A F Lima ,M V Lalic, F, *J. Phys.: Condens. Matte*r 25 (2013) 495505
71. C. He, M. Gu, *Scr Mater* 55 (2006) 481–484.
72. L. Wang, R. Yan, Z. Huo, L. Wang, J. Zeng, J. Bao, X. Wang, Q. Peng, Y. Li, *Angew.Chem. Int. Ed.* **2005**, *44*, 6054.
73. L. Wang,W. Tan, *Nano Lett.* **2006**, *6*, 84.
74. H.-C. Lee, T.-W. Lee, T.-H. Kim, O. O. Park, *Opt. Mater.* **2005**, *27*, 1410.
75. Y. V. Malyukin, S. L. Yefimova, A. N. Lebedenko, A. V. Sorokin, I. A. Borovoy, *J. Lumin.* **2005**, *36*, 439.

76. J. Gass, P. Poddar, J. Almand, S. Srinath, H. Srikanth, *Adv. Funct. Mater.* **2006**, *16*, 71.
77. A.Liu, M. Wei, I. Honma, H. Zhou, *Adv. Funct. Mater.* **2006**, *16*, 371.
78. K. Jin Lee, J. Hak Oh, Y. Kim, J. Jang, *Adv. Mater.* **2006**, *18*, 2216–2219
79. D. Li, J. T. McCann, Y. Xia, M. Marquez, *J. Am. Ceram. Soc.*, 89 [6] 1861–1869 (2006)
80. EM Purcell. *Am Phys Soc* (1946) 69:681.
81. KH Drexhage. *J Lumin* (1970) ;12:693.
82. JJ Macklin, JK Trautman, TD Harris, LE Brus. *Science* (1996) 272, 255.
83. N Danz, J Heber, A Brauer, R.Kowarschik *Phys Rev* A (2002) 66, 063809.
84. K Vasilev, W Knoll, M Kreiter. *J Chem Phys* (2004) 120:3439.
85. H Schniepp, V.Sandoghdar, *Phys Rev Lett* 2002;89:257403.
86. W Lukosz, RE Kunz. *J Opt Soc Am* 1977;67:1607.
87. Kreiter M, Prummer M, Hecht B, Wild UP. *J Chem Phys* 2002;117:9430.
88. C. Oliver, G.M. Pharr, *J. Mater. Res*. 7 (1992) 1564-1583.
89. J. Lakowics, Principles of Fluorescence Spectroscopy, Springer-Verlag, New York, 2006.
90. N. Bras, *Laser Chem.* 10 (1990) 405–412.
91. M.S. Rabasovic, D. Sevic, M. Terzicb, B. P. Marinkovic, *Nucl Instrum Methods Phys Re*s B 279 (2012) 16–19
92. S. Tang, J. Xie, Q. Ma,, *Measurement* 42 (2009) 933–936
93. A. Camposeo, F. Di Benedetto, R. Stabile, A. A. R. Neves,R. Cingolani, D. Pisignano, *Small* (2009), 5, No. 5, 562–566
94. R.M. Dukali, I. Radovic, D.B. Stojanovic, P.S. Uskokovic, N. Romcevic, V. Radojevic, R. Aleksic, *Journal of Alloys and Compounds*, Volume 583, (2014), 376-381
95. S.S. Musbah, V. Radojević, I. Radović, P.S. Uskoković, D.B. Stojanović, M. Dramićanin, R. Aleksić, *J. Min. Metall. Sect. B-Metall.* 48 (2012) 309-318.
96. D. Nagao, T. Kinoshita, A.Watanabeb, M. Konnoa, *Polym Int.* 60 (2011) 1180–1184.

97. K. Okaniwa, Refractive Materials for Interlayer Optical Contacts with TiO2-Based Organic/Inorganic Hybrids, Polymer Engineering and Science (2011) 1637-1641.

98. Particulate Filled Polymer Composites, edited by Roger Rothon, Rapra Technology Limited, Shrewsburry, 2003, pp 11-14.

99. S.D. Kaloshkin, V.V. Tcherdyntsev, M.V. Gorshenkov, V.N. Gulbin, S.A. Kuznetsov, *J. Alloys Compd.* (2012) 536 1 S522-S526

100. H. Chakraborty, A. Sinha, N. Mukherjee, P. P. Chattopadhyay, Exfoliated Graphite Reinforced PMMA Composite: *J Nanotechnol* Volume 2012 Article ID 940516 (2012).

101. H. Wang, Q. Liu, Q. Yang, Y. Li, W. Wang, L. Sun, C. Zhang, Y. Li, *J Mater Sci* **45** (2010) 1032

102. C. Hsu, S. Shivkumar, *Macromol Mater Eng.* **289** 4 (2004) 334

103. T. Jarusuwannapoom, W. Hongrojjanawiwat, S. Jitjaicham, LWannatong, M. Nithitanakul C. Pattamaprom, P. Koombhongse, R. Rangkupan, P. Supaphol, *Eur. Pol. J* **41** 3 (2005) 409

104. I. S. Elashmawi, N. A. Hakeem, *Polym. Eng. Sci.* **48** (2008) 895

105. G. Socrates, *Infrared and Raman Characteristic Group Frequencies*, Wiley, New York, 2001, p. 347

106. A. M. Farag, I. S. Yahia, *Opt. Commun.* **283** (2010) 4310

107. A.V. Deshpande, E. B. Namdas, *J Lumin*. **91** (2000) 25

108. N. Patra, A. C. Barone, M. Salerno, *Adv Pol Tech*, **30**, 1, (2011) 12

109. T. W. J. Gadella, Jr., T. M. Jovin, R. M. Clegg, *Biophys. Chem.* **48** (1993) 2219

110. T. Robinson, Y. Schaerli, R. Wootton, F. Hollfelder, C. Dunsby, G. Baldwin, M. Neil, P. French, A. de Mello, *Lab Chip* **9** (2009) 3437

111. M. F. Al-Kadhemy, I. F. Alsharuee, A. D. Al-Zuky, *J. Physical Sci*. **22** (2011) 77.

Biography

Ramadan Al-Mukhtar Dukali was born on 01. 01. 1964. in Zentani, Libya. During his studies he spent in the UK, where he graduated. Postgraduate studies continued at the Technical University of Gdansk, Poland, where he defended his master's thesis 2000th year. From 1994. -1996. he worked in the Secretariat for Higher Education of the Republic of Libya, Department of Studies abroad and technical cooperation with foreign countries. From 2002.- 2003. he worked at the High Institute of Technology, and from 2004. to 2008. in the Secretariat for Higher Education of the Republic of Libya, the Department for studies abroad and technical cooperation with foreign countries. Since 2010. he is on Faculty of Technology and Metallurgy, University of Belgrade, where he works on developing his doctoral thesis in the field of Materials Engineering.

Biografija

Ramadan Al-Mukhtar Dukali rođen je 01. 01. 1964. godine u Zentanu, Libija. Tokom studija boravio je u Velikoj Britaniji gde je i diplomirao. Posledipolomske studije nastavio je na Tehničkom Univerzitetu u Gdanjsku, Poljska, gde je i odbranio magistarsku tezu 2000. godine. Od 1994-1996. godine radio je u Sekretarijatu za Visoko obrazovanje Republike Libije, Departman za studije u inostranstvu i tehničku saradnju s inostranstvom, Od 2002-2003. je radio na Visokom Institutu Tehnologije, a od 2004-2008. u Sekretarijatu za Visoko obrazovanje Republike Libije, Departman za studije u inostranstvu i tehničku saradnju s inostranstvom. Od 2010. godine je na Tehnološko-metalurškom fakultetu Univerziteta u Beogradu gde radi na izradi svoje doktorske disertacije iz oblasti Inženjerstva materijala.

Appendix 1

Appendix 1.

Изјава о ауторству

Потписани-а **Ramadan Al-Mukhtar Dukali**

број индекса _____

Изјављујем

да је докторска дисертација под насловом

"Синтеза и карактеризација сцинтилационих композитних материјала са полимерном матрицом"

- резултат сопственог истраживачког рада,
- да предложена дисертација у целини ни у деловима није била предложена за добијање било које дипломе према студијским програмима других високошколских установа,
- да су резултати коректно наведени и
- да нисам кршио/ла ауторска права и користио интелектуалну својину других лица.

Потпис докторанда

У Београду, 01.04.2019.

Appendix 2

Appendix 2.

Изјава о истоветности штампане и електронске верзије докторског рада

Име и презиме аутора Рамадан Ал-Мукхтар Дукали

Број индекса

Студијски програм Инжењерство материјала

Наслов рада "Синтеза и карактеризација сцинтилационих композитних материјала са полимерном матрицом"

Ментор Радојевић Весна

Потписани/а др Весна Радојевић, ван. проф.

Изјављујем да је штампана верзија мог докторског рада истоветна електронској верзији коју сам предао/ла за објављивање на порталу **Дигиталног репозиторијума Универзитета у Београду.**

Дозвољавам да се објаве моји лични подаци везани за добијање академског звања доктора наука, као што су име и презиме, година и место рођења и датум одбране рада.

Ови лични подаци могу се објавити на мрежним страницама дигиталне библиотеке, у електронском каталогу и у публикацијама Универзитета у Београду.

Потпис докторанда

У Београду, 01.04.2014.

Appendix 3

Appendix 3.

Изјава о коришћењу

Овлашћујем Универзитетску библиотеку „Светозар Марковић“ да у Дигитални репозиторијум Универзитета у Београду унесе моју докторску дисертацију под насловом:

"Синтеза и карактеризација сцинтилационих композитних материјала са полимерном матрицом"

која је моје ауторско дело.

Дисертацију са свим прилозима предао/ла сам у електронском формату погодном за трајно архивирање.

Моју докторску дисертацију похрањену у Дигитални репозиторијум Универзитета у Београду могу да користе сви који поштују одредбе садржане у одабраном типу лиценце Креативне заједнице (Creative Commons) за коју сам се одлучио/ла.

1. Ауторство

2. Ауторство - некомерцијално

3. Ауторство – некомерцијално – без прераде

4. Ауторство – некомерцијално – делити под истим условима

5. Ауторство – без прераде

6. Ауторство – делити под истим условима

(Молимо да заокружите само једну од шест понуђених лиценци, кратак опис лиценци дат је на полеђини листа).

Потпис докторанда

У Београду, 01.04.2014.

1. Ауторство - Дозвољавате умножавање, дистрибуцију и јавно саопштавање дела, и прераде, ако се наведе име аутора на начин одређен од стране аутора или даваоца лиценце, чак и у комерцијалне сврхе. Ово је најслободнија од свих лиценци.

2. Ауторство – некомерцијално. Дозвољавате умножавање, дистрибуцију и јавно саопштавање дела, и прераде, ако се наведе име аутора на начин одређен од стране аутора или даваоца лиценце. Ова лиценца не дозвољава комерцијалну употребу дела.

3. Ауторство - некомерцијално – без прераде. Дозвољавате умножавање, дистрибуцију и јавно саопштавање дела, без промена, преобликовања или употребе дела у свом делу, ако се наведе име аутора на начин одређен од стране аутора или даваоца лиценце. Ова лиценца не дозвољава комерцијалну употребу дела. У односу на све остале лиценце, овом лиценцом се ограничава највећи обим права коришћења дела.

4. Ауторство - некомерцијално – делити под истим условима. Дозвољавате умножавање, дистрибуцију и јавно саопштавање дела, и прераде, ако се наведе име аутора на начин одређен од стране аутора или даваоца лиценце и ако се прерада дистрибуира под истом или сличном лиценцом. Ова лиценца не дозвољава комерцијалну употребу дела и прерада.

5. Ауторство – без прераде. Дозвољавате умножавање, дистрибуцију и јавно саопштавање дела, без промена, преобликовања или употребе дела у свом делу, ако се наведе име аутора на начин одређен од стране аутора или даваоца лиценце. Ова лиценца дозвољава комерцијалну употребу дела.

6. Ауторство - делити под истим условима. Дозвољавате умножавање, дистрибуцију и јавно саопштавање дела, и прераде, ако се наведе име аутора на начин одређен од стране аутора или даваоца лиценце и ако се прерада дистрибуира под истом или сличном лиценцом. Ова лиценца дозвољава комерцијалну употребу дела и прерада. Слична је софтверским лиценцама, односно лиценцама отвореног кода.